

Optimization of Blood–Brain Barrier Permeability with Potent and Selective Human Neuronal Nitric Oxide Synthase Inhibitors Having a 2-Aminopyridine Scaffold

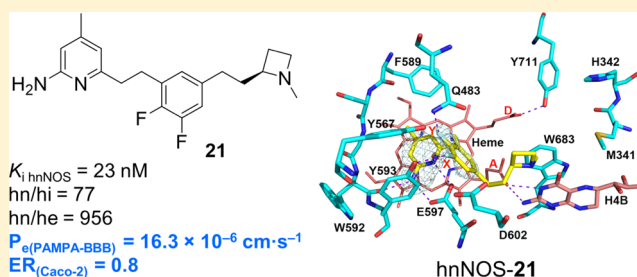
Ha T. Do,[†] Huiying Li,[‡] Georges Chreifi,[‡] Thomas L. Poulos,^{*,‡,§} and Richard B. Silverman^{*,†,§}

[†]Department of Chemistry, Department of Molecular Biosciences, Chemistry of Life Processes Institute, Center for Molecular Innovation and Drug Discovery, Center for Developmental Therapeutics, Northwestern University, 2145 Sheridan Road, Evanston, Illinois 60208-3113, United States

[‡]Departments of Molecular Biology and Biochemistry, Pharmaceutical Sciences, and Chemistry, University of California, Irvine, California 92697-3900, United States

S Supporting Information

ABSTRACT: Effective delivery of therapeutic drugs into the human brain is one of the most challenging tasks in central nervous system drug development because of the blood–brain barrier (BBB). To overcome the BBB, both passive permeability and efflux transporter liability of a compound must be addressed. Herein, we report our optimization related to BBB penetration of neuronal nitric oxide synthase (nNOS) inhibitors toward the development of new drugs for neurodegenerative diseases. Various approaches, including enhancing lipophilicity and rigidity of new inhibitors and modulating the p*K*_a of amino groups, have been employed. In addition to determining inhibitor potency and selectivity, crystal structures of most newly designed compounds complexed to various nitric oxide synthase isoforms have been determined. We have discovered a new analogue (**21**), which exhibits not only excellent potency (*K*_i < 30 nM) in nNOS inhibition but also a significantly low P-glycoprotein and breast-cancer-resistant protein substrate liability as indicated by an efflux ratio of 0.8 in the Caco-2 bidirectional assay.



INTRODUCTION

Neurodegenerative diseases, such as Alzheimer's, Parkinson's, and Huntington's diseases, are characterized by a gradual degeneration and death of neurons in the central nervous system (CNS), causing problems in muscular movements and mental functioning of patients. Despite unmet medical needs, comprehensive treatments for these diseases are still very limited.^{1,2} One of the most difficult challenges in CNS drug development is effective delivery of therapeutic drugs into the human brain, mainly because of the blood–brain barrier (BBB) located at the interface of blood vessels and brain tissues.³ The BBB is composed of a layer of endothelial cells with tight junctions that prevents the access of external toxins and therefore protects the brain and preserves its optimal physiological environment. This cell layer, however, also limits the access of therapeutic drugs into the brain.⁴ The major pathway for CNS drugs to cross the BBB is by passive diffusion through its lipid membrane. In addition to the tight junctions of endothelial cells, high expression levels of efflux transporters, especially P-glycoprotein (P-gp) and breast-cancer-resistant protein (BCRP), contribute greatly to the limited brain exposure of CNS drugs.⁵ Consequently, it becomes necessary in CNS drug development to increase passive permeability and lower P-gp- and BCRP-mediated efflux.^{6,7}

Neuronal nitric oxide synthase (nNOS) has been validated as a promising therapeutic target in the development of new treatments for neurodegenerative diseases.^{8–10} In brain, nitric oxide (NO) produced by nNOS participates in neuronal transmission.¹¹ The overproduction of NO in cells, however, is harmful. In particular, excess NO formed by upregulated nNOS in the CNS can cause excessive nitration and nitrosylation of proteins, leading to their misfolding and aggregation.¹² Additionally, the reaction of NO with superoxide anion creates a strongly oxidizing reagent, peroxynitrite, which, together with reactive oxygen species,^{13,14} damages DNA and causes lipid peroxidation. These processes lead to nerve cell death and impairment in neuronal transmission, which are commonly observed in symptoms of neurodegenerative diseases.^{15,16} Limiting NO production through inhibition of nNOS, therefore, could be an important approach to protect neurons and slow the progression of neurodegenerative diseases.^{17,18}

nNOS is a homodimeric enzyme with each monomer containing one C-terminal reductase domain and one N-terminal oxygenase domain. The C-terminal reductase domain

Received: December 29, 2018

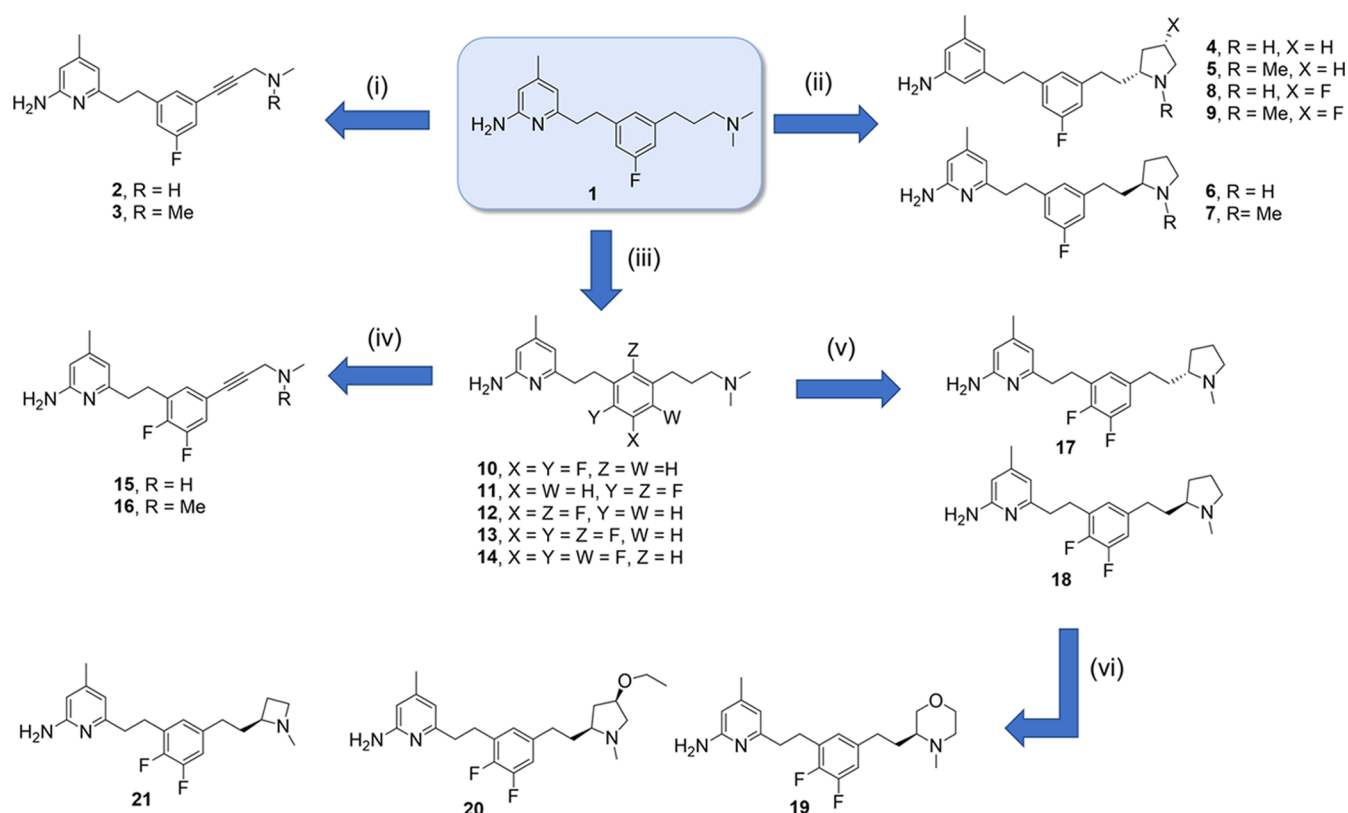


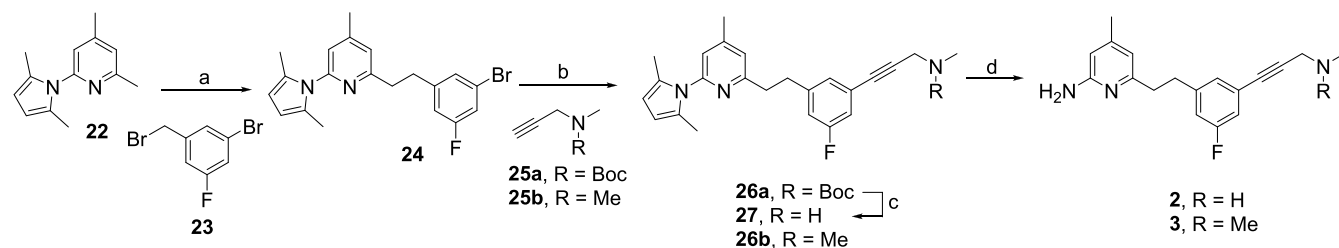
Figure 1. Structural modifications of lead compound **1**: (i) enhancing rigidity with a C–C triple bond; (ii) enhancing lipophilicity and rigidity by incorporating a pyrrolidine ring; (iii) enhancing lipophilicity by incorporating more fluorine atoms into the middle linker; (iv) difluorobenzene linker incorporated with a C–C triple bond; (v) difluorobenzene linker incorporated with a pyrrolidine ring; and (vi) modulating pK_a of the amino tail group.

consists of nicotinamide adenine dinucleotide phosphate (NADPH), flavin adenine dinucleotide, and flavin mononucleotide binding sites, whereas the N-terminal oxygenase domain contains a structural zinc at the dimer interface, a tetrahydrobiopterin (H₄B) cofactor, and a heme as the catalytic center, which is also the substrate, L-arginine (L-Arg), binding site. These two domains are connected to each other by a calmodulin (CaM) binding motif. When CaM is bound in the presence of the calcium influx, electron flow is facilitated from the reductase domain to the heme active site in the oxygenase domain, where L-Arg gets oxidized in a two-step reaction to generate L-citrulline and release NO.^{17,19} Competing against L-Arg binding with a compound at the active site is one of the fundamental approaches to inhibit nNOS.¹⁸ The challenges of this task involve not only inhibitor potency but also selectivity for nNOS over both endothelial NOS (eNOS) and inducible NOS (iNOS), the two isoforms that share very similar structural features in the active site to that of nNOS.^{20,21} It is necessary to avoid over-inhibition of these two nitric oxide synthase (NOS) isoforms since eNOS inhibition can result in cardiovascular failure, whereas iNOS inhibition can cause a disruption in the immune system.²²

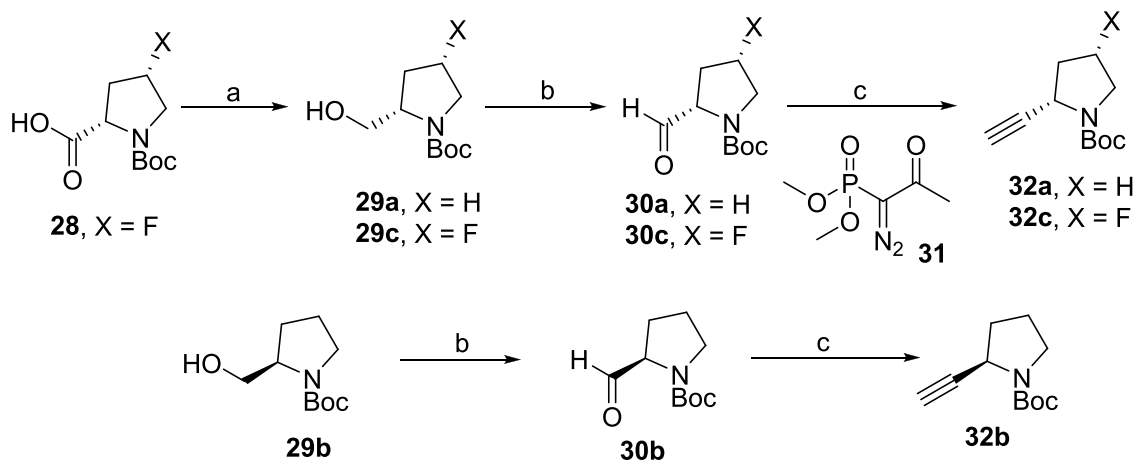
In recent years, our efforts in achieving nNOS inhibitors with excellent potency and high isoform selectivity have led to a promising class of molecules bearing a 2-aminopyridine scaffold. Using this molecular scaffold, we have obtained nNOS inhibitors that exhibit excellent activity at concentrations in the sub-30 nM range.^{17,23,24} Our first generation of nNOS inhibitors bearing a 2-aminopyridine scaffold, however, showed poor predicted permeation through the BBB as revealed by

very little Caco-2 permeability.²⁵ Recently, we have been able to improve cell membrane permeability of our 2-aminopyridine nNOS inhibitors, while retaining their high inhibitory activity. In our previous report, we obtained a new lead compound (**1**, Figure 1), which shows excellent potency and selectivity to human nNOS ($K_i(\text{hnNOS}) = 30 \text{ nM}$; hnNOS/heNOS = 2799) and displays an efflux ratio (ER) of 5.9 in the Caco-2 assay.²⁶ To move forward in CNS drug development, cell membrane permeability of these 2-aminopyridine nNOS inhibitors must be further improved with a required ER of <2.5 for being a likely CNS (+) drug.^{7,27}

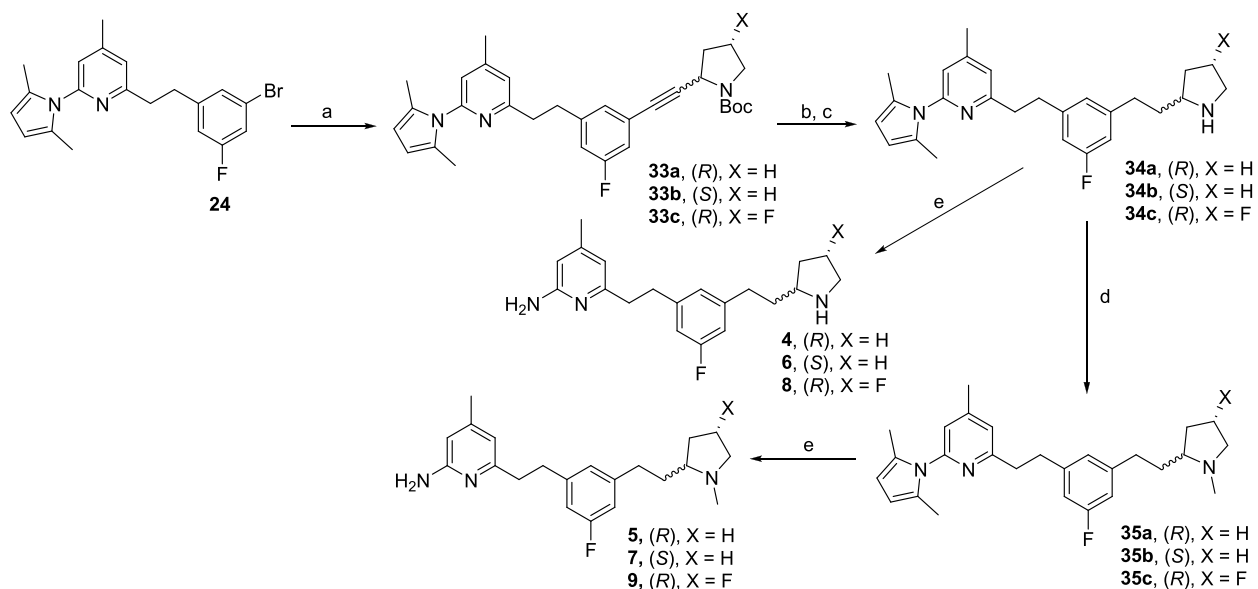
Here, we report our optimization toward improving cell membrane permeability and reducing P-gp and BCRP substrate liability of 2-aminopyridine nNOS inhibitors, using **1** as the lead compound for numerous chemical modifications. Insights into understanding the structural effects on the activity and permeability of analogues have been obtained through various medicinal chemistry approaches, including enhancing the lipophilicity and rigidity of new analogues, along with modulating the pK_a of basic amino groups (Figure 1). These structural modifications have been centralized on enhancing the disposition of nNOS inhibitors into the brain while preserving their potency and selectivity comparable to those of **1**. Moreover, in this work, we aim, for the first time, to investigate the inhibition studies of potential compounds using all human NOS isoforms, which helps to provide not only a direct comparison of isoform selectivity but also more robust data for clinical studies, if any, of the studied nNOS inhibitors should be advanced to a later stage of drug development.

Scheme 1. Synthesis of **2** and **3**^a

^aReagents and conditions: (a) (i) *n*-BuLi 1.6 M/tetrahydrofuran (THF), THF, $-78 \rightarrow -20^\circ\text{C}$, 15 min, (ii) **23**, THF, $-78 \rightarrow -20^\circ\text{C}$, 20 min; (b) **25a** or **25b**, Pd(PPh₃)₄, CuI, triethylamine (TEA)/dimethylformamide (DMF) (9:1), microwave, 120°C , 30 min; (c) 20% trifluoroacetyl (TFA), CH₂Cl₂, room temperature (RT), 1 h; (d) NH₂OH·HCl, EtOH/H₂O (2:1), 100°C , 20 h.

Scheme 2. Synthesis of Pyrrolidinoalkynes^a

^aReagents and conditions: (a) BH₃ 1 M/THF, THF, $0^\circ\text{C} \rightarrow \text{RT}$; (b) Dess–Martin periodinane, CH₂Cl₂, RT, 3 h; (c) **31**, MeOH, RT, 15 h.

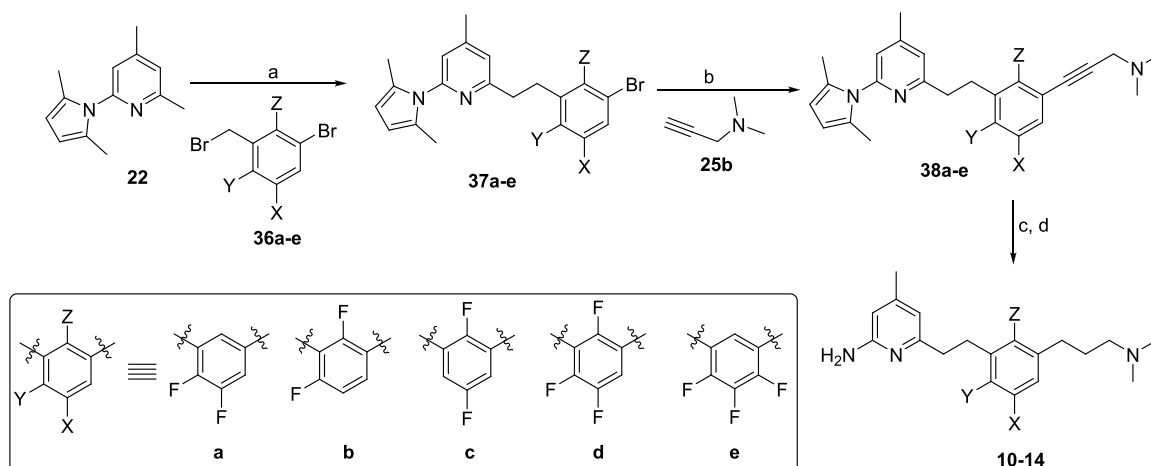
Scheme 3. Synthesis of Pyrrolidine Analogues **4**–**9**^a

^aReagents and conditions: (a) **32a**–**c**, Pd(PPh₃)₄, CuI, TEA/DMF (9:1), microwave, 120°C , 30 min; (b) 20% TFA, CH₂Cl₂, RT, 1 h; (c) Pd/C, H₂, MeOH, RT, 20 h; (d) (i) HCHO 37% in H₂O, (ii) NaBH₄, MeOH; (e) NH₂OH·HCl, EtOH/H₂O (2:1), 100°C , 20 h.

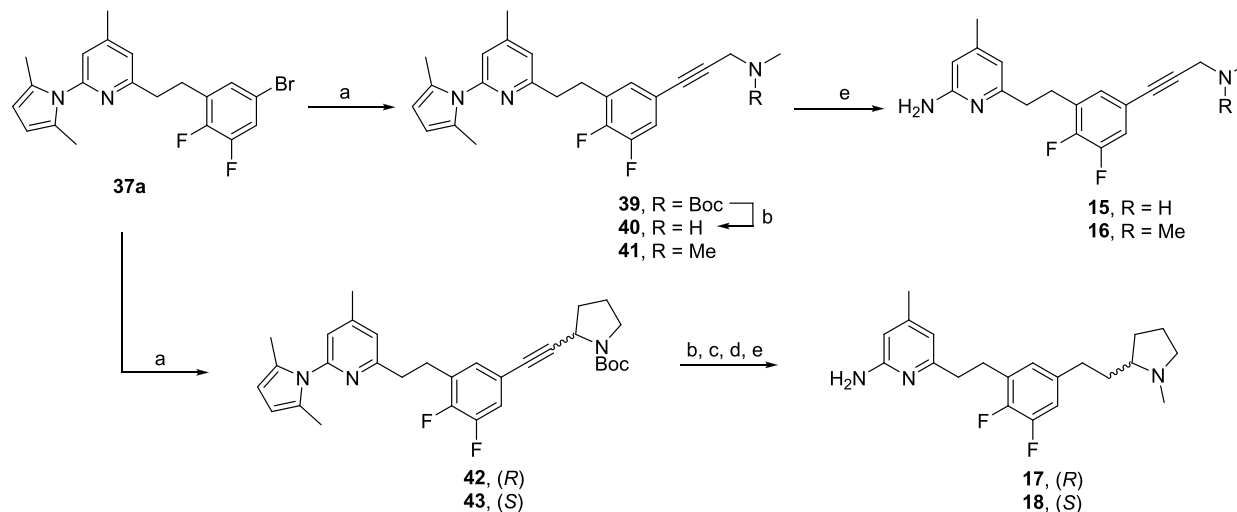
RESULTS AND DISCUSSION

Overall Strategy. While lead compound **1** binds tightly to nNOS and exhibits excellent n/e selectivity, **1** has a high ER (Table 3). To increase brain penetration, molecules were

designed that increased lipophilicity and rigidity of lead compound **1** (Figure 1). Rigidity was increased by adding a C–C triple bond to the tail end to give analogues **2** and **3**. Analogues **4**–**9** with a pyrrolidine ring in the tail introduce

Scheme 4. Synthesis of Di- and Trifluorobenzene Analogues 10–14^a

^aReagents and conditions: (a) (i) *n*-BuLi 1.6 M/THF, THF, $-78 \rightarrow -20$ °C, 15 min, (ii) **36a–e**, THF, $-78 \rightarrow -20$ °C, 20 min; (b) **25b**, Pd(PPh₃)₄, CuI, TEA/DMF (9:1), microwave, 120 °C, 30 min; (c) Pd/C, H₂, MeOH, RT, 20 h; (d) NH₂OH·HCl, EtOH/H₂O (2:1), 100 °C, 20 h.

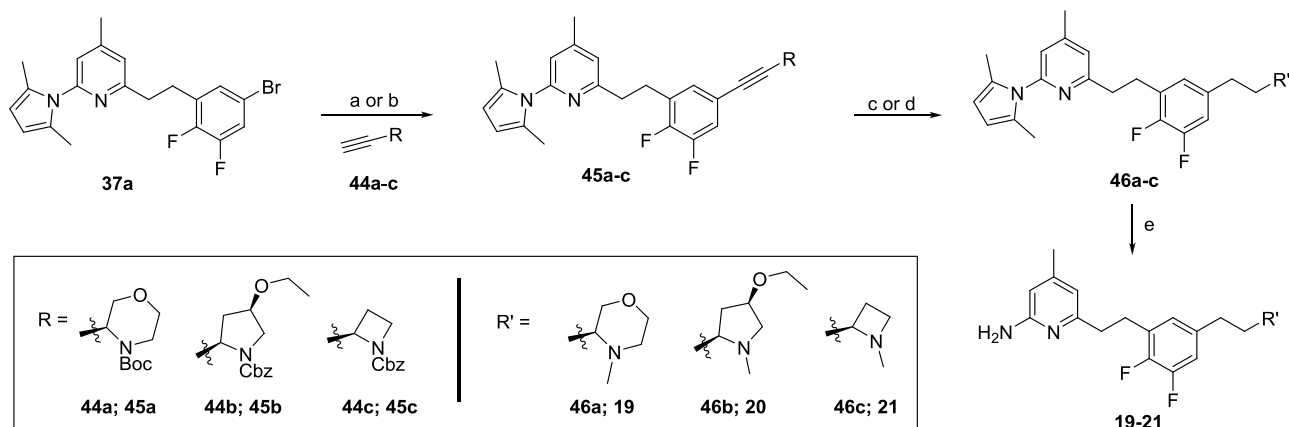
Scheme 5. Synthesis of Analogues 15–18 with Enhanced Lipophilicity and Rigidity^a

^aReagents and conditions: (a) **25a,b** or **32a,b**, Pd(PPh₃)₄, CuI, TEA/DMF (9:1), microwave, 120 °C, 30 min; (b) 20% TFA, CH₂Cl₂, RT, 1 h; (c) Pd/C, H₂, MeOH, RT, 20 h; (d) (i) HCHO 37% in H₂O, (ii) NaBH₄, MeOH; (e) NH₂OH·HCl, EtOH/H₂O (2:1), 100 °C, 20 h.

greater lipophilicity and reduce the number of rotatable bonds. Different enantiomers of the pyrrolidine ring were also studied to investigate the effect of chirality. To increase permeability and decrease metabolism, the pK_a of the tail was decreased by adding a fluorine atom to the C4 position on the pyrrolidine ring (**8** and **9**). The lipophilicity of the new analogues was enhanced by incorporation of additional fluorine atoms onto the middle fluorobenzene linker of **1** (compounds **10–14**). Compounds with an *X,Y*-difluorobenzene linker (**Figure 1**) were identified as the best in both permeability and structural binding properties. Rigidity in the tail was built into **10** to give **15** and **16**. The optimal *X,Y*-difluorobenzene linker was then merged with the pyrrolidine tail in the **4–9** series to give **17** and **18**. Finally, the pK_a of the cyclic amino group, i.e., pyrrolidine ring, in the tail chain was modulated by different heterocycles, including morpholine (**19**) and azetidine (**21**), as well as introducing an electron-withdrawing group into the pyrrolidine ring (**20**). The predicted physicochemical properties of these newly designed compounds can be found in **Table**

S3 in the Supporting Information. All new analogues were tested for nNOS inhibition and selectivity over eNOS and iNOS, whereas cell membrane permeability was investigated using a parallel artificial membrane permeability for blood–brain barrier (PAMPA-BBB) assay. Compounds with high potency, selectivity, and permeability were further examined in a Caco-2 bidirectional assay to evaluate their P-gp and BCRP substrate liability.

Chemistry. The synthesis of compounds **2** and **3** with enhanced rigidity in the tail chain is shown in **Scheme 1**. Deprotonation of pyrrole-protected 2,4-dimethylpyridine **22** by *n*-BuLi followed by a reaction of the generated anion with electrophile **23** provided intermediate **24** with the 2-aminopyridine head and the middle linker coupled. Sonogashira coupling of **24** with either *N*-Boc-*N*-methyl-propargylamine (**25a**) or 3-dimethylamino-1-propyne (**25b**) afforded alkynes carrying a Boc-protected secondary (**26a**) or tertiary (**26b**) amine. Boc-deprotection of **26a** followed by pyrrole depro-

Scheme 6. Synthesis of 19–21^a

^aReagents and conditions: (a) 44a or 44b, Pd(PPh₃)₄, CuI, TEA/DMF (9:1), microwave, 120 °C, 30 min; (b) 44c, Pd(PPh₃)₂Cl₂, CuI, PPh₃, DEA/DMF (1:1), microwave, 120 °C, 20 min; (c) 45a → 46a: (i) 20% TFA, CH₂Cl₂, RT, 1 h, (ii) Pd/C, H₂, MeOH, RT, 20 h, (iii) HCHO 37% in H₂O, NaBH₄, MeOH; (d) 45b,c → 46b,c: (i) Pd(OH)₂/C, H₂ (1 atm), MeOH, RT, 20 h, (ii) HCHO 37% in H₂O, NaBH₄, MeOH; (e) NH₂OH·HCl, EtOH/H₂O (2:1), 100 °C, 20 h.

tection yielded target compound 2, whereas pyrrole deprotection of 26b generated compound 3.

The synthesis of pyrrolidine analogues 4–9 was carried through the preparation of pyrrolidinoalkynes 32a–c (Scheme 2). The pure enantiomers of these pyrrolidinoalkynes were directly synthesized from their corresponding aldehydes (30a–c) using Seyferth–Gilbert homologation. Aldehydes 30a–c were prepared from the oxidation of their corresponding alcohols, obtained from either commercial sources (29a and 29b) or by being synthesized (29c) from a carboxylic acid precursor (28). Scheme 3 shows the synthetic routes for 4–9 from 32a–c. Sonogashira coupling of intermediate 24 with different pyrrolidinoalkynes (32a–c), followed by a sequence of Boc-deprotection and hydrogenation, gave intermediates 34a–c. Pyrrole deprotection of these intermediates provided secondary amine analogues 4, 6, and 8. In a separate pathway, methylation of the secondary amino group using formaldehyde/NaBH₄, followed by a removal of the pyrrole-protecting group, generated tertiary amine analogues 5, 7, and 9.

The synthesis of analogues containing di- and trifluorobenzene linkers (10–14) was started with the preparation of linker components (36a–e) from commercially available sources (see the Supporting Information). Following a general synthetic route for nNOS inhibitors as shown in Scheme 1, the synthesized linkers (36a–e) were coupled with pyrrole-protected 2-aminopyridine head 22 through carbon–carbon bond formation using *n*-BuLi. Generated intermediates (37a–e) then underwent Sonogashira coupling with alkyne 25b to keep the tail chain the same as that of lead compound 1. Alkyne reduction of intermediates 38a–e followed by a pyrrole deprotection yielded desired products 10–14 (Scheme 4).

To obtain the highest possible improvement in cell membrane permeability, a new set of compounds with both enhanced lipophilicity and increased rigidity were synthesized. New analogues were designed to have a difluorobenzene middle linker and a tail chain containing either a pyrrolidine ring or an alkyne amino group in the tail chain to increase their lipophilicity or reduce the number of rotatable bonds, respectively. The synthesis of these analogues (15–18) is shown in Scheme 5. Sonogashira coupling reactions of

previously synthesized 37a with different alkynes (25a,b and 32a,b) yielded intermediates 39 and 41–43. Boc-deprotection of 39 generated intermediate 40, which underwent pyrrole deprotection along with 41 to yield the two desired compounds (15 and 16) bearing the alkyne amino group in the tail chain. On the other hand, 42 and 43 underwent a sequence of reactions, including Boc-deprotection, hydrogenation with Pd/C, methylation with formaldehyde, and pyrrole deprotection, to give the target products (17 and 18) containing a pyrrolidine ring in their tail chain.

The synthesis of compounds 19–21 to modulate the pK_a of the amino group in the tail chain first involved the preparation of the corresponding alkyne-functionalized tail chains (44a–c), whose syntheses can be found in the Supporting Information. Sonogashira coupling again was used to attach these tail chains to intermediate 37a. The target compounds (19–21) were obtained by subsequent reactions including (i) Boc/Cbz deprotection, (ii) hydrogenation of the alkyne, (iii) methylation of the secondary amine to the tertiary amine by HCHO/NaBH₄, and (iv) pyrrole deprotection. It is worth mentioning that these reactions worked efficiently for the synthesis of 19, whereas the removal of the Cbz group in the synthesis of 20 and 21 required the use of Pd(OH)₂/C under H₂ gas. The use of Pd/C, H₂ to remove the Cbz group did not yield the desired products, even at a pressure up to 110 psi hydrogen gas. Additionally, Sonogashira coupling of azetidine alkyne 44c required the use of a different Pd catalyst and base (i.e., Pd(PPh₃)₂Cl₂ and diethylamine, respectively) to obtain a reasonable yield and less inseparable byproducts (Scheme 6).

Biological Activity. The inhibitory activity and selectivity of new analogues 2–21 were determined using the NO hemoglobin (Hb) capture assay, and the results are summarized in Table 1 along with those of lead compound 1. These compounds were first tested against the more easily purified rat and human nNOS and murine iNOS to evaluate potency and selectivity. Relative to 1 with a K_i (hNOS) = 30 nM, eight of the new compounds did not exhibit a significant decrease in potency, eight had a 2- to 3-fold decrease, and four exhibited a 4- to 5-fold decrease in potency. The parallel artificial membrane permeability for blood–brain barrier (PAMPA-BBB) assay was used to evaluate the effects of our

Table 1. Rat and Human nNOS Potency and Effective Permeability (P_e) in the PAMPA-BBB Assay of 1–21^a

compd.	K_i (nM)		hn/rn	P_e (10^{-6} cm s ⁻¹) (PAMPA-BBB)
	rat nNOS	human nNOS		
1	26	30	1.2	14.80 ± 0.69
2	32	58	1.8	15.52 ± 0.02
3	58	124	2.1	18.76 ± 0.03
4	31	68	2.2	5.18 ± 0.05
5	26	52	2.0	13.30 ± 1.44
6	28	59	2.1	5.52 ± 0.22
7	33	84	2.5	13.61 ± 0.24
8	65	129	2.0	12.34 ± 0.06
9	128	204	1.6	18.90 ± 0.08
10	19	29	1.5	15.90 ± 0.48
11	60	36	0.6	15.38 ± 0.50
12	79	157	2.0	16.35 ± 0.44
13	47	58	1.2	18.62 ± 0.20
14	45	46	1.0	18.70 ± 0.20
15	27	43	1.6	18.62 ± 0.48
16	81	84	1.0	18.64 ± 0.31
17	27	37	1.4	17.91 ± 0.60
18	13	21	1.9	17.00 ± 1.00
19	62	89	1.4	21.10 ± 1.12
20	55	87	1.6	17.67 ± 1.80
21	26	23	0.9	16.32 ± 0.35

^a K_i values were calculated from the IC₅₀ values of a dose–response curve using the Cheng–Prusoff equation. Six- to nine concentrations were tested, and the IC₅₀ value was calculated from an average of at least two duplicates. The standard errors were less than 10%. The ratio hn/rn was determined to evaluate the potential translation of these inhibitors from preclinical data to a clinical study. This ratio was aimed to be as close to 1.0 as possible so that there would be little to no significant difference in the amount of inhibitors used in rat and human dosage. The effective permeability (P_e) was obtained after 17 h incubation of a compound through a layer of porcine brain lipid and was reported as an average of triplicate with a standard deviation.

structural modifications on cell membrane permeability of 2–21, which helps to understand the structure–permeability relationship of these compounds. From the PAMPA-BBB assay, a compound is predicted to have a good BBB penetration and is classified as a CNS (+) molecule if its effective permeability (P_e) is larger than 4.0×10^{-6} cm s⁻¹.^{26,28,29} The results in Table 1 reveal that compounds 2–21 exhibit a predicted CNS (+) characteristic, in which 4–8 exhibit lower P_e than that of lead compound 1, whereas 2, 3, and 9–21 display comparable or higher permeability than that of 1. In most cases, the strategies we employed, such as increasing the rigidity of the tail (2 and 3), altering the pK_a of

the tail amine (9), introducing more fluorines (10–14), and combining modulation of pK_a, lipophilicity, and additional fluorines (15–21), help improve permeability. It is evident that subtle changes in structure can result in significant permeability changes. For example, the addition of a single methyl group to 4 and 6 to give 5 and 7, respectively, results in an approximately 2-fold increase in permeability.

The most promising compounds were selected for more detailed analysis by comparing selectivity against the other NOS isoforms, and the results are shown in Table 2.

Efflux Transporter Liability. Because compounds 18 and 21 stand out as the most selective nNOS inhibitors (Table 2) in addition to having excellent cell permeability properties (Table 1), these two compounds were selected for further studies on the potential for BBB penetration. P-glycoprotein (P-gp) and breast-cancer-resistant protein (BCRP) are efflux transporters that are highly expressed at the BBB to remove harmful molecules, including potential drugs, out of the brain.^{5,30} Evaluation of the potential of a compound as an efflux transporter substrate, therefore, is one of the crucial steps in CNS drug development. The P-gp and BCRP substrate liability of a compound can be evaluated through an efflux ratio (ER) obtained from a Caco-2 bidirectional assay,³¹ which measures the ability of compounds to cross a monolayer of colon cells with expressed P-gp and BCRP from two directions, either from apical to basal (A → B) or from basal to apical (B → A) wells. An ER is then determined by a ratio of the apparent permeability (P_{app}) of B → A over A → B. Compounds with an ER larger than 3 are often considered as substrates of P-gp and BCRP with limited retention in the brain.⁷

As shown in Table 3, lead compound 1 has a high efflux ratio (ER = 5.9) and is, therefore, not a good candidate as a

Table 3. Caco-2 Apparent Permeability and Efflux Ratio (ER) of Selected nNOS Inhibitors with Control Compounds

compd.	apparent permeability (P_{app} , 10^{-6} cm s ⁻¹) ^a		efflux ratio
	mean A → B	mean B → A	
1	9.2 ± 0.3	54.2 ± 17.6	5.9
18	1.1 ± 0.1	2.3 ± 0.2	2.1
21	17.05 ± 0.08	13.71 ± 0.07	0.8
metoprolol ^b	37.18	20.39	0.55
atenolol ^c	0.39	0.58	1.47
erythromycin ^d	<0.17	13.39	>78.76

^aApparent permeability value. ^bHigh permeability control. ^cLow permeability control. ^dHigh efflux control.

Table 2. Potency and Selectivity of Selected Compounds with Other NOS Isoforms

compd.	K_i (nM)				selectivity		
	human nNOS	human eNOS	human iNOS	murine iNOS	hnNOS/heNOS	hnNOS/hiNOS	rnNOS/miNOS
1	30	83 976	3501	3857	2756	117	149
10	29	35 028	1312	823	1208	45	43
14	46	50 280	2509	2119	1093	54	47
15	43	16 960	3059	3028	394	71	112
17	37	35 758	1635	2187	966	44	84
18	21	25 548	2222	1290	1216	106	99
21	23	21 980	1780	2060	956	77	79

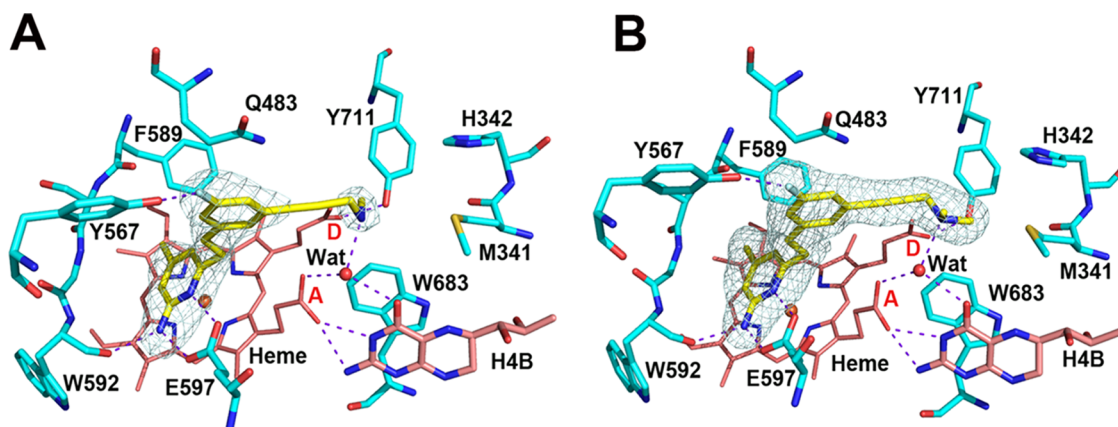


Figure 2. Inhibitor binding environment in the structure of (A) hnNOS-2 (Protein Data Bank (PDB) code: 6NG1) and (B) hnNOS-3 (PDB code: 6NG2). The omit $F_o - F_c$ electron density for the bound ligand is displayed at the contour level of either 2.5σ (regular) or 3.5σ (polder). Major hydrogen bonds are depicted with dashed lines. The heme propionates are labeled in red. This and all other structural figures in this study have similar representations and were prepared with PyMol (www.pymol.org).

CNS drug. Compound **18** gives a substantially improved ER, although membrane penetration is not ideal, whereas compound **21** has excellent membrane penetration and gives a very low ER of 0.8, which compares favorably with the CNS drug, metoprolol, with an ER of 0.55. For comparison, two additional non-CNS drugs are listed in Table 3, both of which exhibit much higher ERs than those of compound **21**.

Structural Analysis: Lead Compound 1. Our early crystallographic work focused on rat nNOS (rnNOS) and bovine eNOS (beNOS), but we have more recently focused on the human isoforms (hnNOS and heNOS). In the current study, a total of 45 crystal structures using the various nNOS and eNOS isoforms have been solved. Here, we focus on a few selected human isoform structures with greater details provided in the Supporting Information. The crystal structure of lead compound **1** complexed with hnNOS and heNOS was previously published, and here, we provide a brief summary relevant to the current study. As with all our inhibitors, the aminopyridine end of **1** stacks over the heme and H-bonds with the buried conserved active site Glu. However, the mode of binding of the rest of **1** is quite different in hnNOS and heNOS (Figure S1). The central fluorobenzene in hnNOS points “up” toward Tyr567, whereas the tail tertiary amine interacts with the H₄B and heme propionate A (Figure S1). The location of the fluorobenzene requires that Gln483 adopts a new rotamer (the “out” rotamer), which places the side chain amide parallel and in contact with the fluorobenzene group. In heNOS, the electron density of **1** is poorly defined, but it nevertheless is clear that the central fluorobenzene ring does not point up but adopts a “bent down” binding mode and lies parallel to the heme. The tertiary amino tail density is poorly defined, suggesting weaker interactions with the heme propionates than in hnNOS. This difference in the orientation of the central fluorobenzene groups is observed in many of the structures solved as part of this study.

Structural Analysis: Rigidifying Lead Compound 1 (Compounds 2 and 3). Rigidifying the tail end of **1** as in compounds **2** and **3** has little effect on the binding mode to hnNOS (Figure 2). The approximately 4-fold lower affinity of **3** relative to that of **1** is most likely associated with the inability of the more rigid tail to maximize electrostatic interactions with heme propionate A. The binding mode changes for **2** and **3** in rnNOS are described in Figure S2.

Structural Analysis: Increasing Lipophilicity (Compounds 4–7). To enhance the lipophilicity of **1** and, therefore, potentially increase its permeability, compounds **4–9**, with a pyrrolidine ring at the tail, were designed and synthesized. Although blocking the H-bonding capability of the pyrrolidine N atom with a methyl group, changing **4** and **6** to **5** and **7**, makes drastic changes in permeability, there is little effect on interactions with the enzyme. Compounds **4** and **5** bind very similarly to that of **1** with the tail pyrrolidine similarly positioned to the tertiary amine of **1** for interactions with heme propionate A (Figure 3A,B). Changing the chirality of the **4** pyrrolidine, however, to give **6** does result in a substantially different binding mode to hnNOS (Figure 3C). Now the pyrrolidine with a different chirality can no longer properly interact with the heme propionates but approaches Asp602 instead. This also requires a fairly substantial repositioning of the central fluorobenzene, which is now roughly perpendicular to the orientation in **4**. These differences have little effect on K_i (Table 1). That these compounds can have such different binding modes yet retain similar potency is likely the result of multiple ways the tail amino group can be stabilized by either the heme propionates or the Asp602 carboxylate. The binding of compounds **4–7** to rnNOS shares more or less the same bent down mode (Figure S3) with the pyrrolidine interacting with heme propionates, which is in agreement with their similar K_i values (Table 1).

Binding of this series of compounds to heNOS provided some surprises. For compounds **4**, **6**, and **8**, two molecules of inhibitor bind (Figure S4). Using **6** as an example (Figure S4B), one **6** molecule binds as expected in the active site but the second **6** molecule binds in the H₄B site such that the aminopyridine of the inhibitor takes the place of the H₄B. This requires Arg365, which normally interacts with the H₄B, to swing out of the way to make room for the second inhibitor molecule. The movement of Arg365 also provides an opening for Zn²⁺ to bind and coordinate with Asp369 and His461 of molecule B of the dimer. We have observed this type of two inhibitor binding together with formation of the Zn²⁺ site in previous studies.³² The new observation from the present study is that the binding of Zn²⁺ is clearly associated with the change in Arg365 and not the displacement of H₄B by a second inhibitor molecule since in the heNOS-9 complex (Figure S4D), a second inhibitor molecule does not bind but

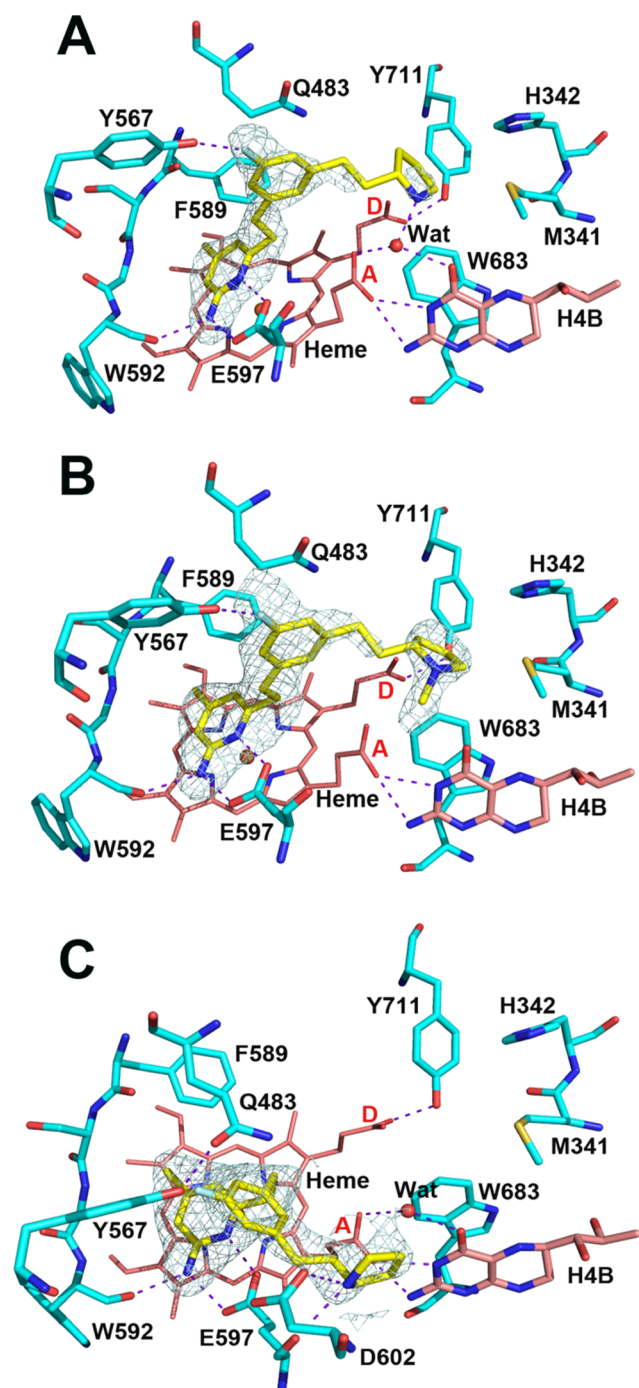


Figure 3. Inhibitor binding environment in the structure of (A) hnNOS-4 (PDB code: 6NG4), (B) hnNOS-5 (PDB code: 6NG5), and (C) hnNOS-6 (PDB code: 6NG6). Note that the binding mode is changed for 4 and 6 because of the chirality difference.

Arg365 still moves, enabling Zn^{2+} to bind. It is quite possible that this Zn^{2+} site is the one associated with the well-known ability of transition metals to inhibit NOS activity.³³ The binding of Zn^{2+} requires disruption of the Arg365–H₄B interaction, and this interaction is known via mutagenesis studies to be essential for NOS activity.³⁴

Addition of Fluorine to Decrease pK_a (Compounds 8 and 9). Structural modifications of compounds that improve permeability may not correlate with inhibitor potency. Analogues that carry a fluorine atom on the pyrrolidine ring,

8 and 9, exhibit much better permeability than that of their parent compounds, 4 or 5, but show a 2-fold and a 4-fold drop, respectively, in both rnNOS and hnNOS inhibitory activities compared with 4 and 5 (Table 1). This reduction is very likely the result of a decrease in the pK_a of the tail amino group, thereby diminishing electrostatic interactions with the heme propionates (Figure 4), which we also found in an earlier study.²⁶ The addition of the fluorine atom to 5 to give 9 also causes a substantial change in binding mode to hnNOS. Although the pyrrolidine of 5 is stabilized by the heme

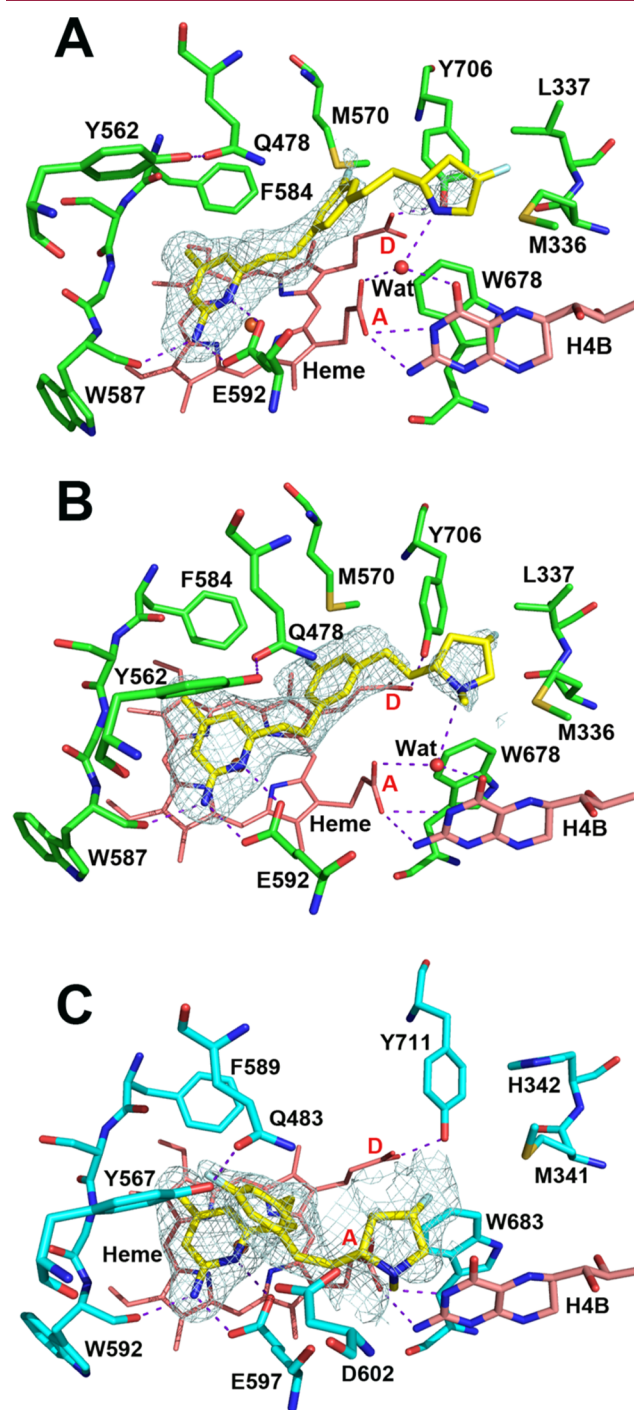


Figure 4. Inhibitor binding environment in the structure of (A) rnNOS-8 (PDB code: 6NGQ), (B) rnNOS-9 (PDB code: 6NGR), and (C) hnNOS-9 (PDB code: 6NG7).

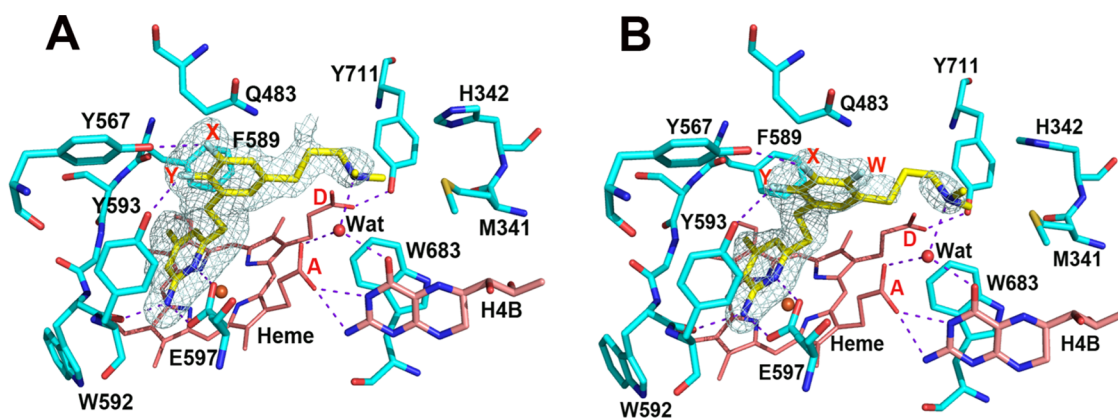


Figure 5. Inhibitor binding environment in the structure of (A) hnNOS-10 (PDB code: 6NG8) and (B) hnNOS-14 (PDB code: 6NGD). The fluorine atom positions on the middle benzene ring are marked in red in this and all following figures.

propionate (Figure 3B), the extra fluorine atom is likely the reason that the pyrrolidine of **9** approaches Asp602 instead of the heme propionate (Figure 4C). The fluorobenzene ring orientation is almost perpendicular to each other in these two modes, the Gln483 being in the “out” or “in” rotamer accordingly. A similar binding mode transition in hnNOS was also observed above from compound **4** to **6** because of the chirality change on the pyrrolidine (Figure 3).

Fluorination of the Central Benzene Linker (Compounds 10–14). To further enhance bioavailability, additional fluorine atoms were added to the middle benzene linker (compounds 10–14), and this caused significant changes in inhibitor binding modes. With compounds where the multiple fluorine atoms are on the same side (W, X, and Y position) of the central benzene ring (**10** and **14**, see Figure 1), the “up” binding mode is very similar to lead compound **1** in hnNOS (Figure 5). In addition, the inhibitory potencies are similar, but the permeability substantially improves, with additional fluorines (compare **1** and **14**, Table 1). When the additional fluorines are on the opposite sides of the benzene ring, the binding mode changes. In **11**, the Y,Z-difluorobenzene ring binds “bent down” and is oriented such that the Y-fluorine is about 3.8 Å from the heme iron for possible electrostatic interactions (Figure 6A). For compound **12**, its central X,Z-difluorobenzene is much farther from the heme iron because the 2-carbon linker from the aminopyridine to difluorobenzene bends in a different way from that in **11** (Figure 6B). Compound **13** shares the same fluorobenzene position with **12**, but the ring flips 180° relative to **13** (Figure 6C). For compounds **11**, **12**, and **13**, electrostatic stabilization of the tail tertiary amino group determines potency. The tail amino group of **11** is near heme propionate D, whereas that of compound **13** is ~3.4 Å from Asp602. The tail tertiary amino group of **12** is not close to any negatively charged group. Therefore, of the 10–14 compounds, **12** has the weakest electrostatic interactions with neighbors, which possibly accounts for the decrease in potency. The changes in binding modes for compounds 10–14 in rnNOS are less dramatic (Figure S5), which are reflected in similar potencies (Table 1).

Building on Compound 10 (Compounds 15–18). On the basis of the information accumulated thus far, **10** was chosen as the scaffold for further modification because of its excellent inhibitory potency and permeability properties. The new analogues were designed with an alkyne amino group (**15**, **16**) or a pyrrolidine ring (**17**, **18**) incorporated in the tail to

reduce the number of rotatable bonds and further increase lipophilicity. We did not attempt to get X-ray crystal data for **16**, but the structures of **15**, **17**, and **18** bound to hnNOS all exhibit very similar “up” binding modes (Figure 7), and the three bound to rnNOS are in the bent down modes (Figure S6). In both cases, the tail amino group is stabilized by its interaction with heme propionate A via a bridging water. Therefore, it is not surprising that the inhibitory potencies of all three are very similar in the low nanomolar range. In the PAMPA-BBB assay, with a rigid alkyne tail, both **15** and **16** show enhanced permeability with P_e values ca. 18×10^{-6} cm s⁻¹.

Modification of Compound 18 (Compounds 19–21). Because of its excellent potency, selectivity, and cell permeability properties, **18** was selected for further modification. Various heterocycles, including morpholine, (4-ethoxy)pyrrolidine, and azetidine, as found in compounds **19**, **20**, and **21**, respectively, were utilized to modulate the basicity of the tertiary amino group of the pyrrolidine ring, which could potentially enhance its permeability and protect it from metabolism.³⁵ Crystal structures show that compounds **18** (Figure 7C) and **19** (Figure 8A) adopt the lead compound **1** binding mode in hnNOS with the tail end of the inhibitor near the heme propionates. The decrease in potency of **19** is very likely the result of the lower pK_a of the morpholine amino group in **19**. On the other hand, compound **19** exhibits the best cell permeability properties with a P_e value of 21.1×10^{-6} cm s⁻¹. This indicates that achieving both good potency and high permeability can be a delicate balance. Although compounds **20** and **21** bind to hnNOS in the “up” mode, the orientation of the central difluorobenzene is almost perpendicular to that found in **18** and **19**, so Gln483 is not required to adopt the “out” rotamer to make room for the inhibitor. The altered difluorobenzene orientation was observed for compounds **6** (Figure 3C) and **9** (Figure 4C) as well. The positions of the tail amino group have two different preferences. For compounds **6** and **9**, the tail amine is near Asp602, which results in rather poor potency, whereas both the (4-ethoxy)pyrrolidine of **20** and the azetidine of **21** are stabilized by heme propionate A. The better binding potency of **21** is possibly the result of higher basicity of its azetidine nitrogen, thereby providing better electrostatic stabilization. Most importantly, compound **21** not only has excellent membrane penetration but also gives a very low ER of 0.8 (Table 3), which means it is potentially a good CNS drug.

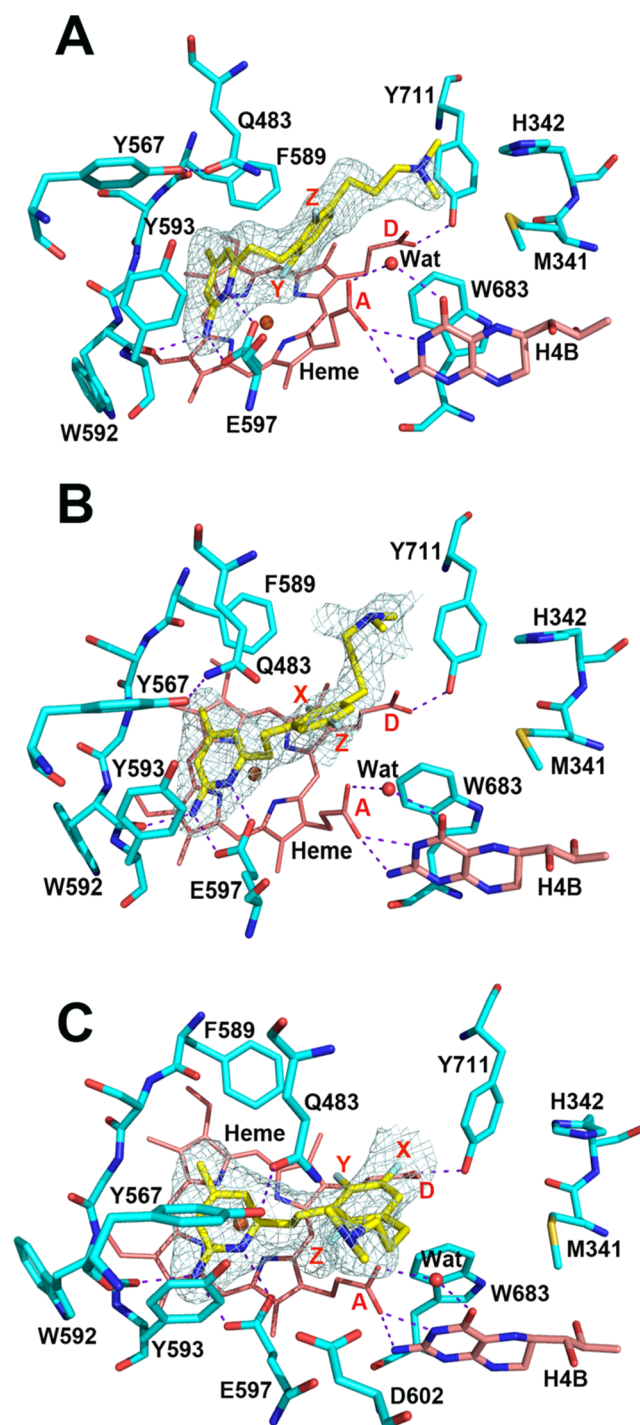


Figure 6. Inhibitor binding environment in the structure of (A) hnNOS-11 (PDB code: 6NGA), (B) hnNOS-12 (PDB code: 6NGB), and (C) hnNOS-13 (PDB code: 6NGC).

In rnNOS, all three compounds bind in the “bent down” mode (Figures S7 and 9A) with their tail ring nitrogen next to propionate A. The variation in potency reflects the strength of this electrostatic interaction.

Isoform Selectivity. In addition to enhancing potency and cell permeability, it is important to retain selectivity for nNOS over the other NOS isoforms, especially eNOS. Because of both potency and bioavailability, six compounds, 10, 14, 15, 17, 18, and 21, were selected for estimating selectivity. With the exception of 15, all of these inhibitors exhibit hnNOS/

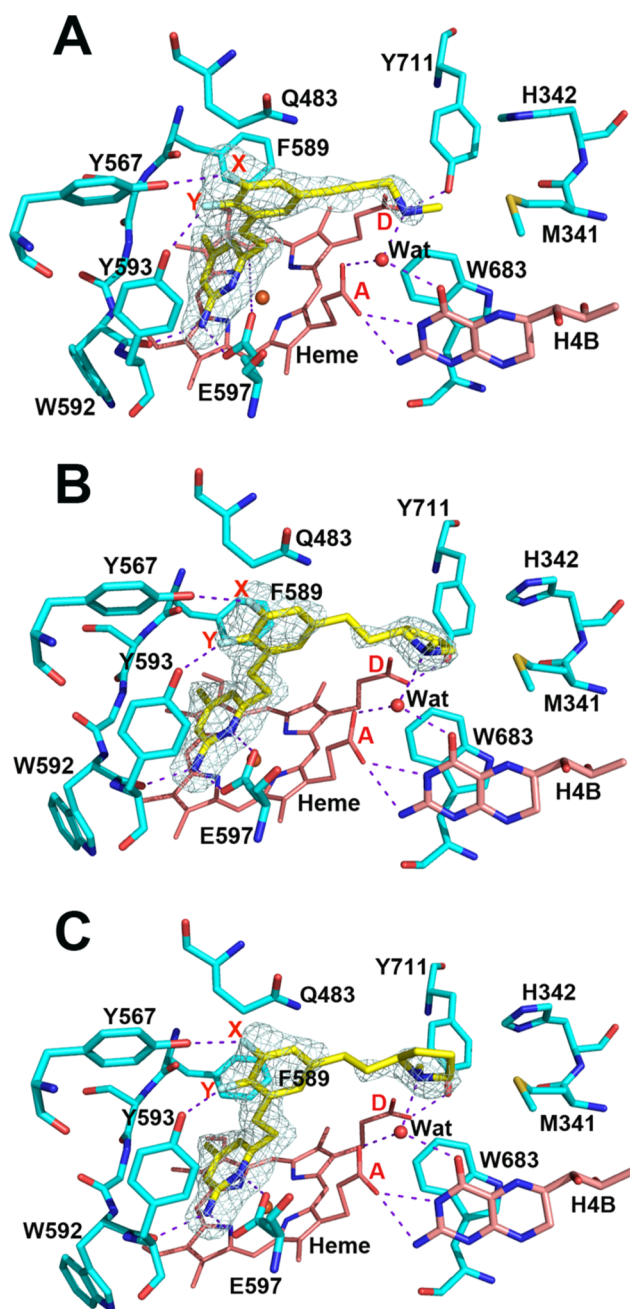


Figure 7. Inhibitor binding environment in the structure of (A) hnNOS-15 (PDB code: 6NGE), (B) hnNOS-17 (PDB code: 6NGF), and (C) hnNOS-18 (PDB code: 6NGH).

heNOS selectivity in the 900–1200 range (Table 2). For human iNOS, the use of the difluorobenzene linker tends to decrease selectivity compared to that of lead compound 1, which is consistent with the observation for rnNOS selectivity over murine iNOS (Table 1). Unlike other analogues, 18 and 21 retain comparable hnNOS/hiNOS selectivity to that of 1.

To understand the structural basis for isoform selectivity, crystal structures of the most selective inhibitors bound to heNOS are required. However, those selective inhibitors that bind poorly to heNOS tend not to give clear electron density. In the series listed in Table 2, the best heNOS crystal structures were obtained for 21. In contrast to the up mode binding of the central difluorobenzene in hnNOS, this ring binds heNOS in the “bent down” mode in contact with the

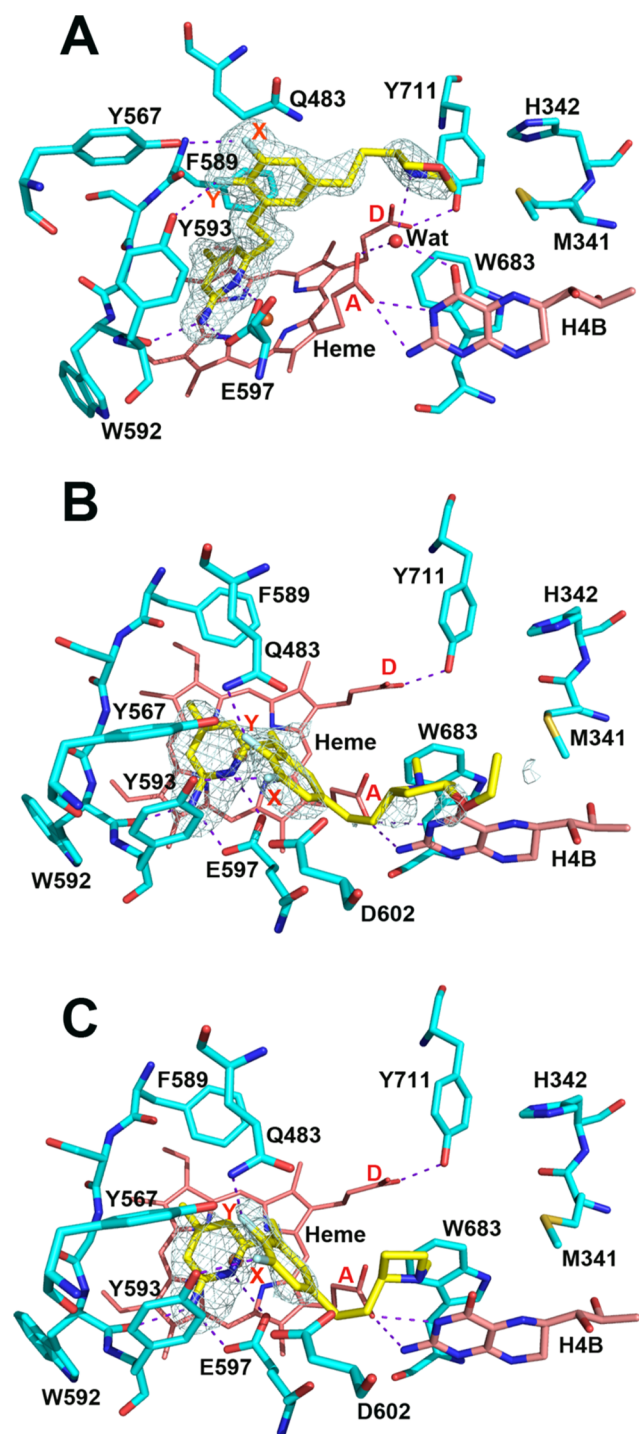


Figure 8. Inhibitor binding environment in the structure of (A) hnNOS-19 (PDB code: 6NGI), (B) hnNOS-20 (PDB code: 6NHB), and (C) hnNOS-21 (PDB code: 6NHC).

heme propionates. As noted earlier, all of the compounds in the current study also bind to rnNOS in the bent down mode. This “up” and “bent down” difference has little to do with potency between hnNOS and rnNOS (Table 1). What requires explanation is why **21** exhibits a hnNOS/heNOS selectivity of 956 as well as high rnNOS/heNOS selectivity. Although **21** binds to both rnNOS and heNOS in a bent down mode, the exact position of the central difluorobenzene is quite different (Figure 9A,B, respectively). Although the benzene ring in rnNOS is sequestered within the arm of heme

propionate D with close contacts with heme and Met570, the benzene in heNOS sits above two propionates. The reason behind this preference lies in the amino acid differences nearby. Where heNOS has Val104 and Phe105, rnNOS has Met336 and Leu337 (Met341 and His342 in hnNOS). The larger Met336 in rnNOS allows good van der Waals contacts with the methyl group of the azetidine, placing the latter near heme propionate A, whereas the contact with the bulky Phe105 in heNOS pulls the azetidine the opposite way. On the other hand, the tail azetidine of **21** in hnNOS comes within 3.8 Å of heme propionate A. Therefore, in both rnNOS and hnNOS, the **21** tertiary amine tail interacts more favorably with heme propionate A than in heNOS, resulting in better potency and n/e selectivity.

CONCLUSIONS

In summary, we report our optimization of nNOS inhibitors bearing a 2-aminopyridine scaffold with emphasis on improving cell membrane permeability of these inhibitors to be able to cross the blood–brain barrier, while retaining excellent inhibition activity and high isoform selectivity. A new series of potent and selective human nNOS inhibitors have been designed and synthesized by employing various medicinal chemistry approaches involving enhancing the lipophilicity, increasing molecular rigidity, and modulating the pK_a of the basic amino tail group of lead molecule **1**. Crystal structures show that the central fluorobenzene can adopt quite different orientations in the active site, but this variability does not alter the binding affinity between hnNOS and rnNOS. As in previous studies, affinity differences are controlled mainly by electrostatic and van der Waals interactions with the tail end of the inhibitor. The most promising inhibitor, **21**, with one additional fluorine atom on the fluorobenzene middle linker compared with lead compound **1** and an azetidine ring in the tail displays excellent inhibition for human nNOS ($K_i = 23$ nM) and high selectivity over human eNOS (hn/he = 956) and human iNOS (hn/hi = 77) but also exhibits a great potential of brain penetration. Caco-2 bidirectional assays reveal that **21** has an efflux ratio of only 0.8, which is significantly lower than that of lead compound **1** (ER = 5.9) and the suggested ER of <2.5 for CNS (+) drugs. The Caco-2 bidirectional assay also revealed that **21** has high cell membrane permeability with the P_{app} value of 17.0×10^{-6} cm s⁻¹, which is in good agreement with the effective permeability ($P_e = 16.3 \times 10^{-6}$ cm s⁻¹) determined by the PAMPA-BBB assay. Our results herein provide the basis for further exploration of the 2-aminopyridine nNOS inhibitors in CNS drug development and additional insights into the strategies to overcome the BBB using medicinal chemistry approaches.

EXPERIMENTAL SECTION

Chemistry. General Procedures. All reagents, unless specified, were obtained from Sigma-Aldrich, Combi-blocks, and Oakwood Chemical Companies. Anhydrous solvents (THF, CH₂Cl₂, MeCN, and DMF) were purified before use by passing through a column composed of activated alumina and a supported copper redox catalyst. Sonogashira coupling was carried out in the Biotage Initiator microwave using Biotage microwave vials (0.5–2, 2–5, and 10–20 mL). Thin-layer chromatography was performed on silica gel 60 F254 precoated plates (0.25 mm) from SiliCycle, and components were visualized by ultraviolet light (254 nm) and/or KMnO₄ or ninhydrin stain. Flash column chromatography was performed on an Agilent 971-FP automated flash purification system with a Varian column

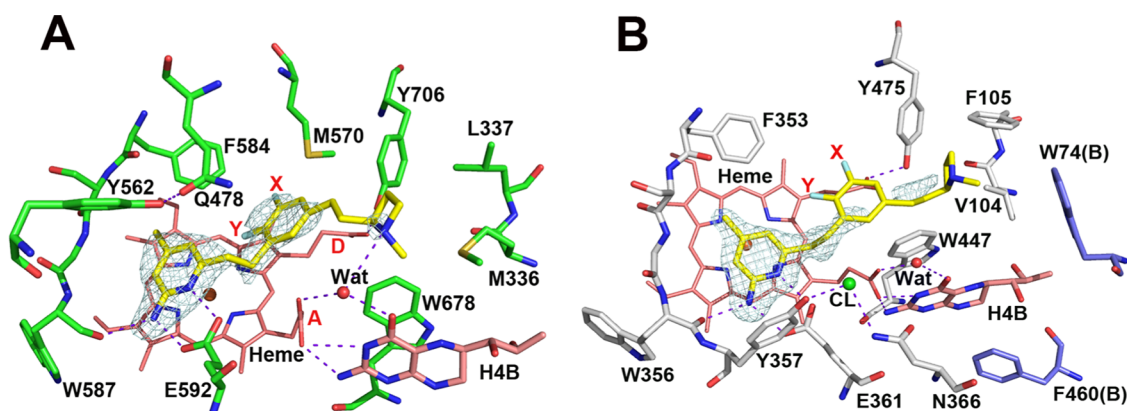


Figure 9. Inhibitor binding environment in the structure of (A) mnNOS-21 (PDB code: 6NHD) and (B) heNOS-21 (PDB code: 6NHF).

station and various SiliCycle cartridges (4–80 g, 40–63 μ m, 60 Å). ^1H and ^{13}C NMR spectra were recorded on a Bruker Avance-III NMR spectrometer at 500 and 126 MHz, respectively, in CDCl_3 or CD_3OD . Chemical shifts were reported in parts per million, multiplicities are indicated by s = singlet, d = doublet, t = triplet, q = quartet, sep = septet, dd = doublet of doublet, dt = doublet of triplet, m = multiplet, and br = broad resonance. Coupling constants “J” were reported in hertz. High-resolution mass spectral (HRMS) data were obtained on an Agilent 6210 LC-TOF spectrometer in the positive ion mode using electrospray ionization (ESI) with an Agilent G1312A high-performance liquid chromatography (HPLC) pump and an Agilent G1367B autoinjector at the Integrated Molecular Structure Education and Research Center (IMSERC), Northwestern University. The purity of compounds was tested using a reserved-phase analytical Agilent Infinity 1260 HPLC with an Agilent Poroshell 120 EC-C18 column, detecting with UV absorbance at 254 nm. All compounds undergoing biological testing were >95% pure.

General Procedure A: Pyrrole Deprotection. In a microwave vial, starting materials **26b** or **41** (1 equiv) and $\text{NH}_2\text{OH}\cdot\text{HCl}$ (3–4 equiv) were added. They are diluted with EtOH/water (2:1) to form a 0.16 M solution. The microwave vial was capped, and the reaction mixture was run at 100 $^\circ\text{C}$ for 20 h. The cap was removed, and the reaction mixture was concentrated under reduced pressure. The crude product mixture was purified by reversed flash chromatography to give final products **3** or **16**.

General Procedure B: Boc and Pyrrole Deprotection. The starting material **26a** or **39** (1 equiv) was dissolved in CH_2Cl_2 (0.1 M), followed by the addition of TFA (1.1 equiv) at 0 $^\circ\text{C}$, and the reaction was run at RT. After stirring at RT for 1 h, the crude product was concentrated under reduced pressure, diluted back with CH_2Cl_2 , and washed with sat. NaHCO_3 . The organic layer was dried over Na_2SO_4 and concentrated to give crude products, which were submitted to pyrrole deprotection following the protocol in general procedure A to give **2** or **15**.

General Procedure C: Alkyne Reduction and Pyrrole Deprotection. The starting material **38a–e** (1 equiv) was dissolved in MeOH (0.1 M). The solution was degassed for 5 min, and 10 wt % Pd/C was added. The reaction was run at RT for 20 h under a hydrogen balloon (1 atm). The crude mixture was then filtered through a pad of celite, and the filtrate was concentrated under reduced pressure. Without any purification, the crude product was subjected to the pyrrole deprotection following the protocol in general procedure A to give **10–14**.

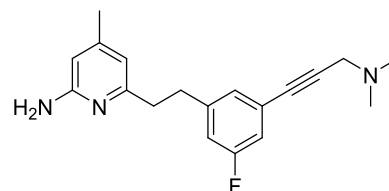
General Procedure D: Boc-Deprotection, Alkyne Reduction, Reductive Amination, and Pyrrole Deprotection. The starting material (**33a–c**, **42**, **43**, or **45a**) was dissolved in CH_2Cl_2 (0.1 M), and TFA (1.1 equiv) was added at 0 $^\circ\text{C}$. The reaction was run at RT for 1 h; then, the solvent and TFA were removed under reduced pressure. The crude mixture was diluted back with CH_2Cl_2 and washed with saturated Na_2CO_3 . The organic layer was then

concentrated, and a crude product was subjected to an alkyne reduction without any purification.

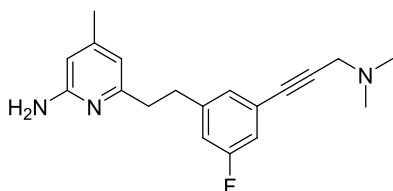
The crude product (1 equiv) was dissolved in MeOH (0.1 M), and the solution was degassed for 5 min, followed by an addition of 10 wt % Pd/C. The reaction was run at RT for 20 h under a hydrogen balloon (1 atm). The crude mixture was then filtered through a pad of celite, and the filtrate was concentrated under reduced pressure.

The crude reduction product was diluted with MeOH (0.24 M), followed by an addition of 37% HCHO in H_2O (3 equiv). The reaction was run at RT for 5 min. The reaction was brought to 0 $^\circ\text{C}$, and NaBH_4 (3 equiv) was added slowly. The reaction was further run for 2 h at RT. Upon completion, the reaction was quenched with water, and the methanol was removed under reduced pressure. The aqueous mixture was extracted with ethyl acetate three times, and the organic layers were combined, dried over Na_2SO_4 , and concentrated to give the crude product, which was subjected to pyrrole deprotection without any purification using the protocol in general procedure A to give **5**, **7**, **9**, **17**, **18**, and **19**. For compounds **4**, **6**, and **8**, which carry only the secondary amine in the tail, the syntheses followed the same protocol except the reductive amination with HCHO was omitted.

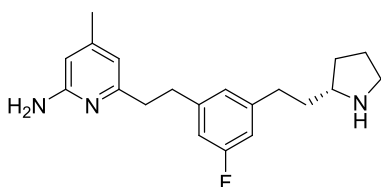
General Procedure E: Cbz Deprotection, Reductive Amination, and Pyrrole Deprotection. The starting material (**45b,c**, 1 equiv) was dissolved in MeOH (0.1 M). The solution was degassed for 5 min, and 10% $\text{Pd}(\text{OH})_2/\text{C}$ was added. The reaction was run at RT for 24 h under a hydrogen balloon (1 atm). After completion, the reaction mixture was filtered through a pad of celite, and the filtrate was concentrated under reduced pressure to give the crude product, which was subjected to reductive amination with formaldehyde and pyrrole deprotection following the same protocols described in general procedure D to give **20–21**.



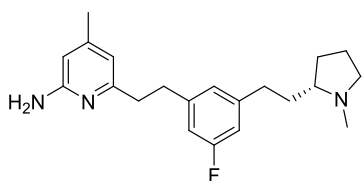
6-(3-Fluoro-5-(3-(methylamino)prop-1-yn-1-yl)phenethyl)-4-methylpyridin-2-amine (2). Compound **2** (74 mg, 50% for two steps) was prepared from **26b** (237 mg, 0.5 mmol) according to general procedure B. ^1H NMR (500 MHz, CD_3OD) δ 7.08 (s, 1H), 6.98–6.91 (m, 2H), 6.29 (s, 1H), 6.27 (s, 1H), 3.58 (s, 2H), 2.92 (dd, $J = 6.5, 9.4$ Hz, 2H), 2.79 (dd, $J = 6.3, 9.2$ Hz, 2H), 2.48 (s, 3H), 2.17 (s, 3H). ^{13}C NMR (126 MHz, CD_3OD) δ 162.4 (d, $J_{\text{C-F}} = 246.2$ Hz), 157.6, 154.4, 147.9, 143.2 (d, $J_{\text{C-F}} = 8.1$ Hz), 127.8 (d, $J_{\text{C-F}} = 2.9$ Hz), 123.1 (d, $J_{\text{C-F}} = 10.1$ Hz), 116.5 (d, $J_{\text{C-F}} = 21.5$ Hz), 116.3 (d, $J_{\text{C-F}} = 23.5$ Hz), 113.6, 109.6, 86.5 (d, $J_{\text{C-F}} = 3.6$ Hz), 79.3, 38.0, 33.7, 33.6, 31.5, 20.6. HRMS-ESI: calculated for $\text{C}_{18}\text{H}_{20}\text{FN}_3$ [$\text{M} + \text{H}$] $^+$ 298.1714, found 298.1716.



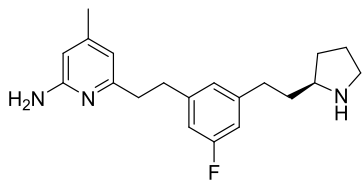
6-(3-(3-(Dimethylamino)prop-1-yn-1-yl)-5-fluorophenethyl)-4-methylpyridin-2-amine (3). Compound 3 (132 mg, 90%) was prepared from **26b** (184 mg, 0.47 mmol) according to general procedure A. ^1H NMR (500 MHz, CD_3OD) δ 7.34 (s, 1H), 7.23–7.14 (m, 2H), 6.69 (s, 1H), 6.62 (s, 1H), 4.36 (s, 2H), 3.38–3.28 (m, 2H), 3.13–2.97 (m, 8H), 2.36 (s, 3H). ^{13}C NMR (126 MHz, CD_3OD) δ 166.4 (d, $J_{\text{C-F}} = 246.4$ Hz), 161.6, 158.4, 151.9, 147.2 (d, $J_{\text{C-F}} = 8.1$ Hz), 131.8 (d, $J_{\text{C-F}} = 2.8$ Hz), 126.7 (d, $J_{\text{C-F}} = 10.2$ Hz), 120.8 (d, $J_{\text{C-F}} = 21.8$ Hz), 120.4 (d, $J_{\text{C-F}} = 23.7$ Hz), 117.5, 113.5, 92.1 (d, $J_{\text{C-F}} = 3.5$ Hz), 81.8, 69.4, 45.5 (2C), 37.6, 37.5, 24.5. HRMS-ESI: calculated for $\text{C}_{19}\text{H}_{22}\text{FN}_3$ $[\text{M} + \text{H}]^+$ 312.1871, found 312.1874.



(R)-6-(3-Fluoro-5-(2-(pyrrolidin-2-yl)ethyl)phenethyl)-4-methylpyridin-2-amine (4). Compound 4 (78 mg, 33% for three steps) was prepared from **33a** (362 mg, 0.7 mmol) according to general procedure D. ^1H NMR (500 MHz, CD_3OD) δ 7.06 (s, 1H), 6.94–6.86 (m, 2H), 6.68 (s, 1H), 6.63 (s, 1H), 3.56–3.50 (m, 1H), 3.36–3.34 (m, 1H), 3.23 (q, $J = 7.3$ Hz, 1H), 3.11–2.98 (m, 4H), 2.76 (t, $J = 8.0$ Hz, 2H), 2.36 (s, 3H), 2.31–2.22 (m, 1H), 2.17–1.94 (m, 4H), 1.79–1.66 (m, 1H). ^{13}C NMR (126 MHz, CD_3OD) δ 161.5 (d, $J_{\text{C-F}} = 244.8$ Hz), 156.1, 152.9, 146.8, 141.8 (d, $J_{\text{C-F}} = 7.8$ Hz), 141.0 (d, $J_{\text{C-F}} = 7.9$ Hz), 122.7, 112.1, 111.4 (d, $J_{\text{C-F}} = 21.6$ Hz), 111.3 (d, $J_{\text{C-F}} = 21.4$ Hz), 107.9, 58.5, 43.3, 32.5, 32.4, 31.9, 30.5, 28.2, 21.6, 19.0. HRMS-ESI: calculated for $\text{C}_{20}\text{H}_{26}\text{FN}_3$ $[\text{M} + \text{H}]^+$ 328.2184, found 328.2185.

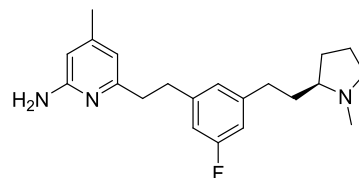


(R)-6-(3-Fluoro-5-(2-(1-methylpyrrolidin-2-yl)ethyl)phenethyl)-4-methylpyridin-2-amine (5). Compound 5 (41 mg, 15% for four steps) was prepared from **33a** (401 mg, 0.8 mmol) according to general procedure D. ^1H NMR (500 MHz, CD_3OD) δ 7.06 (s, 1H), 6.91 (dd, $J = 9.6, 20.1$ Hz, 2H), 6.68 (s, 1H), 6.63 (s, 1H), 3.72–3.68 (m, 1H), 3.37–3.36 (m, 1H), 3.23–3.12 (m, 1H), 3.09–2.99 (m, 4H), 2.94 (s, 3H), 2.84–2.67 (m, 2H), 2.47–2.38 (m, 1H), 2.36 (s, 3H), 2.34–2.27 (m, 1H), 2.22–2.03 (m, 2H), 1.97–1.78 (m, 2H). ^{13}C NMR (126 MHz, CD_3OD) δ 163.1 (d, $J_{\text{C-F}} = 244.7$ Hz), 157.7, 154.4, 148.4, 143.3 (d, $J_{\text{C-F}} = 7.5$ Hz), 142.6 (d, $J_{\text{C-F}} = 7.8$ Hz), 124.2, 113.6, 113.0 (d, $J_{\text{C-F}} = 21.4$ Hz), 112.8 (d, $J_{\text{C-F}} = 21.6$ Hz), 109.5, 68.7, 55.9, 38.5, 34.0, 33.9, 31.9, 31.7, 29.2, 21.1, 20.5. HRMS-ESI: calculated for $\text{C}_{21}\text{H}_{28}\text{FN}_3$ $[\text{M} + \text{H}]^+$ 342.2340, found 342.2342.

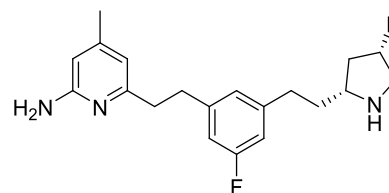


(S)-6-(3-Fluoro-5-(2-(pyrrolidin-2-yl)ethyl)phenethyl)-4-methylpyridin-2-amine (6). Compound 6 (47 mg, 28% for three steps) was prepared from **33b** (257 mg, 0.5 mmol) according to general

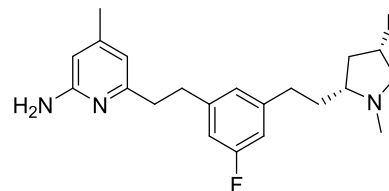
procedure D. ^1H NMR (500 MHz, CD_3OD) δ 7.05 (s, 1H), 6.89 (t, $J = 10.9$ Hz, 2H), 6.68 (s, 1H), 6.63 (s, 1H), 3.59–3.45 (m, 2H), 3.40–3.34 (m, 1H), 3.10–2.98 (m, 4H), 2.76 (t, $J = 8.0$ Hz, 2H), 2.36 (s, 3H), 2.32–2.23 (m, 1H), 2.18–1.91 (m, 4H), 1.79–1.62 (m, 1H). ^{13}C NMR (126 MHz, CD_3OD) δ 163.1 (d, $J_{\text{C-F}} = 244.9$ Hz), 157.7, 154.4, 148.4, 143.4 (d, $J_{\text{C-F}} = 7.8$ Hz), 142.6 (d, $J_{\text{C-F}} = 7.8$ Hz), 124.2, 113.6, 112.9 (d, $J_{\text{C-F}} = 21.8$ Hz), 112.8 (d, $J_{\text{C-F}} = 21.6$ Hz), 109.4, 60.1, 44.9, 34.0, 33.9, 33.4, 32.0, 29.7, 23.1, 20.5. HRMS-ESI: calculated for $\text{C}_{20}\text{H}_{26}\text{FN}_3$ $[\text{M} + \text{H}]^+$ 328.2184, found 328.2180.



(S)-6-(3-Fluoro-5-(2-(1-methylpyrrolidin-2-yl)ethyl)phenethyl)-4-methylpyridin-2-amine (7). Compound 7 (42 mg, 24% for four steps) was prepared from **33b** (257 mg, 0.5 mmol) according to general procedure D. ^1H NMR (500 MHz, CD_3OD) δ 7.07 (s, 1H), 6.95–6.88 (m, 2H), 6.70 (s, 1H), 6.63 (s, 1H), 3.71 (ddd, $J = 5.0, 8.0, 11.5$ Hz, 1H), 3.34–3.30 (m, 1H), 3.17 (dt, $J = 8.4, 11.4$ Hz, 1H), 3.05 (s, 4H), 2.94 (s, 3H), 2.84–2.67 (m, 2H), 2.45–2.38 (m, 1H), 2.36 (s, 3H), 2.33–2.26 (m, 1H), 2.21–2.04 (m, 2H), 1.98–1.80 (m, 2H). ^{13}C NMR (126 MHz, CD_3OD) δ 163.0 (d, $J_{\text{C-F}} = 244.7$ Hz), 157.6, 154.4, 148.3, 143.4 (d, $J_{\text{C-F}} = 7.8$ Hz), 142.6 (d, $J_{\text{C-F}} = 7.8$ Hz), 124.2, 113.6, 113.0 (d, $J_{\text{C-F}} = 21.4$ Hz), 112.8 (d, $J_{\text{C-F}} = 21.6$ Hz), 109.5, 68.7, 55.9, 38.5, 34.1, 33.9, 31.9, 31.7, 29.3, 21.1, 20.6. HRMS-ESI: calculated for $\text{C}_{21}\text{H}_{28}\text{FN}_3$ $[\text{M} + \text{H}]^+$ 342.2340, found 342.2341.

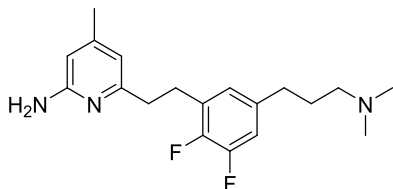


6-(3-Fluoro-5-(2-((2R,4S)-4-fluoropyrrolidin-2-yl)ethyl)phenethyl)-4-methylpyridin-2-amine (8). Compound 8 (62 mg, 30% for three steps) was prepared from **33c** (310 mg, 0.6 mmol) according to general procedure D. ^1H NMR (500 MHz, CD_3OD) δ 7.08 (s, 1H), 6.88 (dd, $J = 17.5, 9.6$ Hz, 2H), 6.69 (s, 1H), 6.61 (s, 1H), 5.44 (dt, $J = 3.4, 52.3$ Hz, 1H), 3.89–3.80 (m, 1H), 3.71 (ddd, $J = 3.9, 13.9, 34.7$ Hz, 1H), 3.64–3.49 (m, 1H), 3.09–2.99 (m, 4H), 2.85–2.71 (m, 2H), 2.60–2.48 (m, 1H), 2.34 (s, 3H), 2.20 (ddt, $J = 7.0, 9.3, 14.0$ Hz, 1H), 2.14–1.91 (m, 2H). ^{13}C NMR (126 MHz, CD_3OD) δ 162.9 (d, $J_{\text{C-F}} = 244.5$ Hz), 157.5, 154.2, 148.2, 143.0 (d, $J_{\text{C-F}} = 7.4$ Hz), 142.4 (d, $J_{\text{C-F}} = 7.6$ Hz), 124.1, 113.5, 112.9 (d, $J_{\text{C-F}} = 21.6$ Hz), 112.8 (d, $J_{\text{C-F}} = 21.8$ Hz), 109.4, 91.9 (d, $J_{\text{C-F}} = 175.9$ Hz), 58.5, 51.0 (d, $J_{\text{C-F}} = 24.7$ Hz), 37.5 (d, $J_{\text{C-F}} = 20.9$ Hz), 33.9, 33.8, 32.9, 31.9, 20.5. HRMS-ESI: calculated for $\text{C}_{20}\text{H}_{25}\text{F}_2\text{N}_3$ $[\text{M} + \text{H}]^+$ 346.2089, found 346.2088.

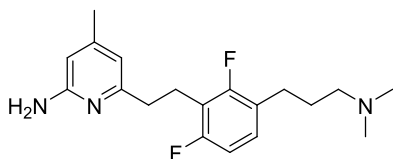


6-(3-Fluoro-5-(2-((2R,4S)-4-fluoro-1-methylpyrrolidin-2-yl)ethyl)phenethyl)-4-methylpyridin-2-amine (9). Compound 9 (30 mg, 24% for four steps) was prepared from **33c** (180 mg, 0.35 mmol) according to general procedure D. ^1H NMR (500 MHz, CD_3OD) δ 7.08 (s, 1H), 6.94 (d, $J = 9.9$ Hz, 1H), 6.90 (d, $J = 9.7$ Hz, 1H), 6.68 (s, 1H), 6.64 (s, 1H), 5.45 (dd, $J = 5.1, 52.5$ Hz, 1H), 3.94 (t, $J = 15.0$ Hz, 1H), 3.58–3.46 (m, 2H), 3.07–3.03 (m, 4H), 3.02 (s, 3H), 2.97–2.69 (m, 3H), 2.36 (s, 3H), 2.24–2.09 (m, 2H), 2.01–1.94 (m, 1H). ^{13}C NMR (126 MHz, CD_3OD) δ 163.1 (d, $J_{\text{C-F}} = 244.7$ Hz),

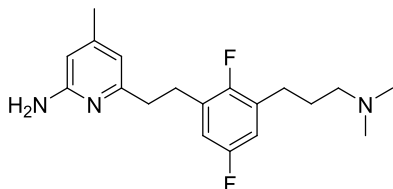
157.6, 154.4, 148.3, 143.0 (d, J_{C-F} = 7.7 Hz), 142.7 (d, J_{C-F} = 7.7 Hz), 124.2, 113.6, 113.0 (d, J_{C-F} = 21.4 Hz), 112.9 (d, J_{C-F} = 21.6 Hz), 109.5, 90.6 (d, J_{C-F} = 176.0 Hz), 67.5, 61.6 (d, J_{C-F} = 23.5 Hz), 38.4, 36.8 (d, J_{C-F} = 22.7 Hz), 34.1, 33.9, 32.6, 31.5, 20.5. HRMS-ESI: calculated for $C_{21}H_{27}F_2N_3$ [$M + H$]⁺ 360.2246, found 360.2246.



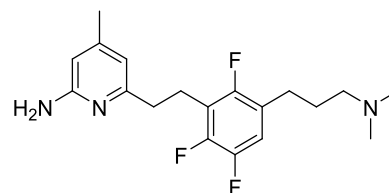
6-(5-(3-(Dimethylamino)propyl)-2,3-difluorophenethyl)-4-methylpyridin-2-amine (10). Compound **10** (25 mg, 39% for two steps) was prepared from **38a** (80 mg, 0.2 mmol) according to general procedure C. ¹H NMR (500 MHz, CD₃OD) δ 7.13–7.06 (m, 2H), 6.71 (s, 1H), 6.60 (s, 1H), 3.21–3.15 (m, 2H), 3.15–3.03 (m, 4H), 2.92 (s, 6H), 2.70 (t, J = 7.7 Hz, 2H), 2.36 (s, 3H), 2.11–2.01 (m, 2H). ¹³C NMR (126 MHz, CD₃OD) δ 157.6, 154.4, 150.1 (dd, J_{C-F} = 246.6, 13.3 Hz), 147.9, 147.3 (dd, J_{C-F} = 244.4, 12.6 Hz), 137.4–137.2 (m), 128.7 (d, J_{C-F} = 12.5 Hz), 125.3 (t, J_{C-F} = 3.0 Hz), 115.3 (d, J_{C-F} = 17.5 Hz), 113.6, 109.6, 56.9, 42.1, 32.7, 31.1, 27.5, 25.7, 20.5. HRMS-ESI: calculated for $C_{19}H_{25}F_2N_3$ [$M + H$]⁺ 334.2089, found 334.2089.



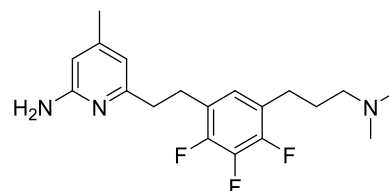
6-(3-(3-(Dimethylamino)propyl)-2,6-difluorophenethyl)-4-methylpyridin-2-amine (11). Compound **11** (35 mg, 35% for two steps) was prepared from **38b** (122 mg, 0.3 mmol) according to general procedure C. ¹H NMR (500 MHz, CD₃OD) δ 7.27 (q, J = 7.9 Hz, 1H), 6.91 (t, J = 8.8 Hz, 1H), 6.73 (s, 1H), 6.49 (s, 1H), 3.24–3.19 (m, 2H), 3.14 (t, J = 7.3 Hz, 2H), 3.02 (t, J = 7.3 Hz, 2H), 2.92 (s, 6H), 2.73 (t, J = 7.7 Hz, 2H), 2.32 (s, 3H), 2.04 (t, J = 8.2 Hz, 2H). ¹³C NMR (126 MHz, CD₃OD) δ 160.0 (dd, J_{C-F} = 244.8, 8.2 Hz), 159.2 (dd, J_{C-F} = 245.6, 8.2 Hz), 157.5, 154.4, 147.8, 129.3 (dd, J = 6.6, 10.0 Hz), 123.0 (dd, J = 3.7, 17.0 Hz), 114.4 (t, J = 20.6 Hz), 113.7, 110.7 (dd, J = 3.6, 22.3 Hz), 109.7, 56.9, 42.1, 31.9, 25.1 (d, J = 2.4 Hz), 24.8, 21.4, 20.5. HRMS-ESI: calculated for $C_{19}H_{25}F_2N_3$ [$M + H$]⁺ 334.2089, found 334.2090.



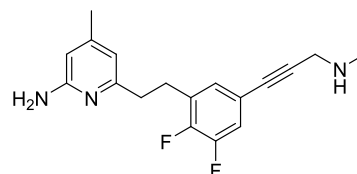
6-(3-(3-(Dimethylamino)propyl)-2,5-difluorophenethyl)-4-methylpyridin-2-amine (12). Compound **12** (32 mg, 42% for two steps) was prepared from **38c** (93 mg, 0.23 mmol) according to general procedure C. ¹H NMR (500 MHz, CD₃OD) δ 7.11–6.92 (m, 2H), 6.72 (s, 1H), 6.59 (s, 1H), 3.25–3.18 (m, 2H), 3.14–3.01 (m, 4H), 2.92 (s, 6H), 2.75 (t, J = 7.9 Hz, 2H), 2.36 (s, 3H), 2.13–2.01 (m, 2H). ¹³C NMR (126 MHz, CD₃OD) δ 158.4 (d, J_{C-F} = 242 Hz), 157.6, 155.2 (d, J_{C-F} = 241 Hz), 154.4, 147.9, 128.9 (dd, J = 8.1, 19.2 Hz), 128.2 (dd, J = 8.2, 19.3 Hz), 115.0 (ddd, J = 4.7, 20.3, 24.5 Hz, 2C), 113.6, 109.6, 56.9, 42.1, 32.5, 27.7, 25.4, 24.5, 20.6. HRMS-ESI: calculated for $C_{19}H_{25}F_2N_3$ [$M + H$]⁺ 334.2089, found 334.2092.



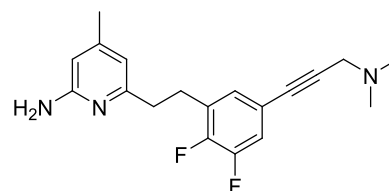
6-(3-(3-(Dimethylamino)propyl)-2,5,6-trifluorophenethyl)-4-methylpyridin-2-amine (13). Compound **13** (10 mg, 24% for two steps) was prepared from **38d** (50 mg, 0.12 mmol) according to general procedure C. ¹H NMR (500 MHz, CD₃OD) δ 7.24 (ddd, J = 6.9, 8.8, 10.6 Hz, 1H), 6.71 (s, 1H), 6.54 (s, 1H), 3.23–3.13 (m, 4H), 3.03 (t, J = 7.4 Hz, 2H), 2.91 (s, 6H), 2.73 (t, J = 7.8 Hz, 2H), 2.34 (s, 3H), 2.08–1.96 (m, 2H). ¹³C NMR (126 MHz, CD₃OD) δ 156.1, 153.0, 152.9 (ddd, J_{C-F} = 1.3, 5.0, 242.0 Hz), 146.0, 145.8 (ddd, J_{C-F} = 8.8, 13.9, 245.7 Hz), 145.1 (ddd, J_{C-F} = 2.5, 12.6, 244.4 Hz), 121.9 (dt, J_{C-F} = 5.1, 19.2 Hz), 115.2 (dd, J_{C-F} = 16.6, 23.1 Hz), 114.5 (dd, J_{C-F} = 5.9, 19.5 Hz), 112.2, 108.3, 55.3, 40.6, 30.2, 23.3, 23.0, 20.2, 19.0. HRMS-ESI: calculated for $C_{19}H_{24}F_3N_3$ [$M + H$]⁺ 352.1995, found 352.1996.



6-(5-(3-(Dimethylamino)propyl)-2,3,4-trifluorophenethyl)-4-methylpyridin-2-amine (14). Compound **14** (48 mg, 36% for two steps) was prepared from **38e** (160 mg, 0.37 mmol) according to general procedure C. ¹H NMR (500 MHz, CD₃OD) δ 7.15 (td, J = 7.6, 2.4 Hz, 1H), 6.64 (s, 1H), 6.58 (s, 1H), 3.24–3.16 (m, 2H), 3.12–2.98 (m, 4H), 2.91 (s, 6H), 2.77 (t, J = 7.7 Hz, 2H), 2.34 (s, 3H), 2.11–2.01 (m, 2H). ¹³C NMR (126 MHz, CD₃OD) δ 156.5, 155.2, 149.3, 148.1 (dd, J_{C-F} = 245.7, 10.1 Hz, 2C), 139.6 (td, J_{C-F} = 250.7, 16.4 Hz), 124.8 (dd, J_{C-F} = 7.6, 3.8 Hz), 124.3 (dd, J_{C-F} = 13.9, 5.0 Hz), 124.0 (dd, J_{C-F} = 13.9, 3.8 Hz), 113.6, 109.2, 56.8, 42.1, 33.4, 27.4, 24.7, 24.6, 20.4. HRMS-ESI: calculated for $C_{19}H_{24}F_3N_3$ [$M + H$]⁺ 352.1995, found 352.1997.

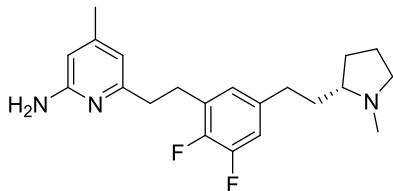


6-(2,3-Difluoro-5-(3-(methylamino)prop-1-yn-1-yl)phenethyl)-4-methylpyridin-2-amine (15). Compound **15** (80 mg, 63% for two steps) was prepared from **39** (198 mg, 0.4 mmol) according to general procedure B. ¹H NMR (500 MHz, CD₃OD) δ 7.42–7.33 (m, 2H), 6.72 (s, 1H), 6.59 (s, 1H), 4.18 (s, 2H), 3.16 (dd, J = 6.3, 9.0 Hz, 2H), 3.06 (dd, J = 6.2, 9.0 Hz, 2H), 2.85 (s, 3H), 2.35 (s, 3H). ¹³C NMR (126 MHz, CD₃OD) δ 157.6, 154.5, 149.9 (dd, J_{C-F} = 248.4, 13.6 Hz), 149.6 (dd, J_{C-F} = 250.6, 13.0 Hz), 147.5, 129.8 (d, J_{C-F} = 13.5 Hz), 129.6–129.4 (m), 118.9 (d, J_{C-F} = 19.3 Hz), 117.9–117.8 (m), 113.6, 109.8, 85.7, 79.1, 38.0, 32.4, 31.5, 27.2, 20.5. HRMS-ESI: calculated for $C_{18}H_{19}F_2N_3$ [$M + H$]⁺ 316.1620, found 316.1618.

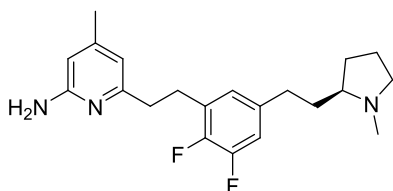


6-(5-(3-(Dimethylamino)prop-1-yn-1-yl)-2,3-difluorophenethyl)-4-methylpyridin-2-amine (16). Compound **16** (65 mg, 66%) was prepared from **41** (122 mg, 0.3 mmol) according to general procedure

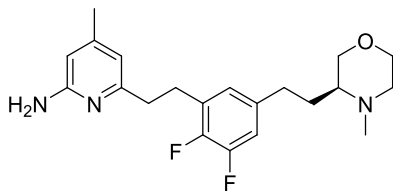
A. ^1H NMR (500 MHz, CD_3OD) δ 7.45–7.38 (m, 2H), 6.70 (s, 1H), 6.60 (s, 1H), 4.35 (s, 2H), 3.15 (t, J = 7.7 Hz, 2H), 3.10–2.98 (m, 8H), 2.36 (s, 3H). ^{13}C NMR (126 MHz, CD_3OD) δ 157.7, 154.5, 150.0 (dd, $J_{\text{C-F}}$ = 248.8, 13.7 Hz), 149.8 (dd, $J_{\text{C-F}}$ = 250.9, 12.9 Hz), 147.6, 129.8 (d, $J_{\text{C-F}}$ = 13.5 Hz), 129.7 (t, $J_{\text{C-F}}$ = 3.5 Hz), 119.1 (d, $J_{\text{C-F}}$ = 19.5 Hz), 117.5 (dd, $J_{\text{C-F}}$ = 8.8, 4.7 Hz), 113.6, 109.8, 87.4, 77.7, 46.9, 41.5 (2C), 32.4, 27.2, 20.5. HRMS-ESI: calculated for $\text{C}_{19}\text{H}_{21}\text{F}_2\text{N}_3$ $[\text{M} + \text{H}]^+$ 330.1776, found 330.1777.



(*R*)-6-(2,3-Difluoro-5-(2-(1-methylpyrrolidin-2-yl)ethyl)phenethyl)-4-methylpyridin-2-amine (**17**). Compound **17** (55 mg, 46% for four steps) was prepared from **42** (173 mg, 0.33 mmol) according to general procedure D. ^1H NMR (500 MHz, MeOD) δ 7.18–7.06 (m, 2H), 6.71 (s, 1H), 6.60 (s, 1H), 3.77–3.67 (m, 1H), 3.35–3.30 (m, 1H), 3.21–3.15 (m, 1H), 3.15–3.02 (m, 4H), 2.95 (s, 3H), 2.79–2.65 (m, 2H), 2.47–2.38 (m, 1H), 2.36 (s, 3H), 2.33–2.24 (m, 1H), 2.22–2.03 (m, 2H), 1.95–1.80 (m, 2H). ^{13}C NMR (126 MHz, MeOD) δ 157.6, 154.4, 150.1 (dd, $J_{\text{C-F}}$ = 246.9, 13.0 Hz), 147.9, 147.3 (dd, $J_{\text{C-F}}$ = 244.4, 13.9 Hz), 137.8–137.1 (m), 128.7 (d, $J_{\text{C-F}}$ = 12.4 Hz), 125.3 (d, $J_{\text{C-F}}$ = 3.2 Hz), 115.2 (d, $J_{\text{C-F}}$ = 17.3 Hz), 113.6, 109.6, 68.6, 55.9, 38.5, 32.7, 31.9, 31.2, 29.2, 27.5, 21.1, 20.5. HRMS-ESI: calculated for $\text{C}_{21}\text{H}_{27}\text{F}_2\text{N}_3$ $[\text{M} + \text{H}]^+$ 360.2246, found 360.2247.

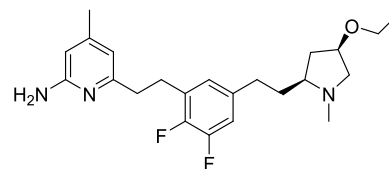


(*S*)-6-(2,3-Difluoro-5-(2-(1-methylpyrrolidin-2-yl)ethyl)phenethyl)-phenethyl-4-methylpyridin-2-amine (**18**). Compound **18** (64 mg, 38% for four steps) was prepared from **43** (244 mg, 0.47 mmol) according to general procedure D. ^1H NMR (500 MHz, CD_3OD) δ 7.15–7.07 (m, 2H), 6.70 (s, 1H), 6.60 (s, 1H), 3.71 (ddd, J = 5.0, 8.0, 11.6 Hz, 1H), 3.21–3.09 (m, 4H), 3.05 (dd, J = 6.6, 9.3 Hz, 2H), 2.95 (s, 3H), 2.80–2.63 (m, 2H), 2.46–2.38 (m, 1H), 2.34–2.24 (m, 1H), 2.21–2.04 (m, 2H), 1.94–1.80 (m, 2H). ^{13}C NMR (126 MHz, CD_3OD) δ 157.7, 154.4, 150.1 (dd, $J_{\text{C-F}}$ = 246.8, 13.4 Hz), 147.9, 147.3 (dd, $J_{\text{C-F}}$ = 244.4, 13.9 Hz), 137.5, 128.7 (d, $J_{\text{C-F}}$ = 12.5 Hz), 125.2, 115.2 (d, $J_{\text{C-F}}$ = 17.3 Hz), 113.6, 109.6, 68.7, 55.9, 38.5, 32.7, 31.9, 31.2, 29.2, 27.5, 21.1, 20.5. HRMS-ESI: calculated for $\text{C}_{21}\text{H}_{27}\text{F}_2\text{N}_3$ $[\text{M} + \text{H}]^+$ 360.2246, found 360.2245.

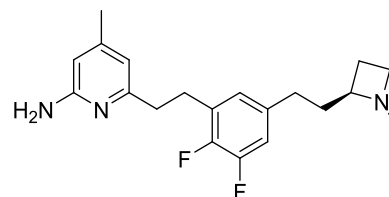


(*S*)-6-(2,3-Difluoro-5-(2-(4-methylmorpholin-3-yl)ethyl)phenethyl)-phenethyl-4-methylpyridin-2-amine (**19**). Compound **19** (68 mg, 28% for four steps) was prepared from **45a** (346 mg, 0.65 mmol) according to general procedure D. ^1H NMR (500 MHz, CD_3OD) δ 7.19–7.03 (m, 2H), 6.70 (s, 1H), 6.59 (s, 1H), 4.15 (dd, J = 13.2, 3.5 Hz, 1H), 4.09–4.01 (m, 1H), 3.93–3.77 (m, 1H), 3.63 (dd, J = 13.2, 10.4 Hz, 1H), 3.50 (dd, J = 12.9, 2.2 Hz, 1H), 3.30–3.25 (m, 1H), 3.17–3.02 (m, 4H), 2.99 (s, 3H), 2.80–2.59 (m, 2H), 2.36 (s, 3H), 2.32–2.23 (m, 1H), 1.93–1.78 (m, 1H). ^{13}C NMR (126 MHz, CD_3OD) δ 157.7, 154.4, 150.1 (dd, $J_{\text{C-F}}$ = 248.2, 13.9 Hz), 147.9, 147.4 (dd, $J_{\text{C-F}}$ = 244.4, 12.6 Hz), 137.2 (d, $J_{\text{C-F}}$ = 5.0 Hz), 128.8 (d, $J_{\text{C-F}}$ = 12.5 Hz), 125.3 (d, $J_{\text{C-F}}$ = 3.3 Hz), 115.3 (d, $J_{\text{C-F}}$ = 17.8 Hz),

113.6, 109.6, 67.6, 63.7, 63.3, 54.0, 39.9, 32.7, 30.1, 28.0, 27.5, 20.5. HRMS-ESI: calculated for $\text{C}_{21}\text{H}_{27}\text{F}_2\text{N}_3\text{O}$ $[\text{M} + \text{H}]^+$ 376.2195, found 376.2197.



6-(5-(2-((2*S*,4*R*)-4-Ethoxy-1-methylpyrrolidin-2-yl)ethyl)-2,3-difluorophenethyl)-4-methylpyridin-2-amine (**20**). Compound **20** (22 mg, 41% for three steps) was prepared from **45b** (75 mg, 0.13 mmol) according to general procedure E. ^1H NMR (500 MHz, CD_3OD) δ 6.96 (ddd, J = 11.3, 7.3, 2.2 Hz, 1H), 6.82 (t, J = 5.1, 2.2 Hz, 1H), 6.28 (s, 1H), 6.27 (s, 1H), 3.98 (td, J = 6.6, 6.1, 3.5 Hz, 1H), 3.47 (q, J = 6.9 Hz, 2H), 3.18 (d, J = 11.0 Hz, 1H), 3.00 (t, J = 7.8 Hz, 2H), 2.82 (d, J = 7.8 Hz, 2H), 2.68–2.59 (m, 1H), 2.54–2.47 (m, 1H), 2.42 (dt, J = 13.5, 7.4 Hz, 1H), 2.35 (dd, J = 11.0, 5.8 Hz, 1H), 2.31 (s, 3H), 2.17 (s, 3H), 2.06–1.97 (m, 1H), 1.60–1.51 (m, 2H), 1.19 (t, J = 7.0 Hz, 3H). ^{13}C NMR (126 MHz, CD_3OD) δ 159.3, 157.5, 150.1 (dd, $J_{\text{C-F}}$ = 245.6, 13.3 Hz), 149.7, 147.0 (dd, $J_{\text{C-F}}$ = 242.9, 12.8 Hz), 138.3 (d, $J_{\text{C-F}}$ = 5.2 Hz), 130.3 (d, $J_{\text{C-F}}$ = 12.7 Hz), 125.1 (t, $J_{\text{C-F}}$ = 3.3 Hz), 114.2 (d, $J_{\text{C-F}}$ = 17.3 Hz), 113.2, 106.7, 76.3, 65.4, 63.9, 62.2, 39.0, 38.4, 37.3, 34.4, 31.6, 28.6, 19.6, 14.3. HRMS-ESI: calculated for $\text{C}_{23}\text{H}_{31}\text{F}_2\text{N}_3\text{O}$ $[\text{M} + \text{H}]^+$ 404.2508, found 404.2510.



(*S*)-6-(2,3-Difluoro-5-(2-(1-methylazetidin-2-yl)ethyl)phenethyl)-4-methylpyridin-2-amine (**21**). Compound **21** (15 mg, 11% for three steps) was prepared from **45c** (213 mg, 0.4 mmol) according to general procedure E. ^1H NMR (500 MHz, CD_3OD) δ 6.93 (ddd, J = 11.3, 7.3, 2.2 Hz, 1H), 6.79 (d, J = 6.1 Hz, 1H), 6.27 (s, 2H), 3.38 (td, J = 7.7, 2.3 Hz, 1H), 3.05 (qd, J = 7.9, 5.9 Hz, 1H), 2.99 (t, J = 7.8 Hz, 2H), 2.89–2.84 (m, 1H), 2.82 (d, J = 7.8 Hz, 2H), 2.58–2.45 (m, 2H), 2.32 (s, 3H), 2.17 (s, 3H), 2.08–2.01 (m, 1H), 1.93–1.84 (m, 1H), 1.83–1.67 (m, 2H). ^{13}C NMR (126 MHz, CD_3OD) δ 159.4, 157.6, 150.1 (dd, $J_{\text{C-F}}$ = 245.6, 13.2 Hz), 149.6, 147.0 (dd, $J_{\text{C-F}}$ = 242.9, 12.8 Hz), 138.2–138.1 (m), 130.3 (d, $J_{\text{C-F}}$ = 12.7 Hz), 125.1 (t, $J_{\text{C-F}}$ = 3.2 Hz), 114.2 (d, $J_{\text{C-F}}$ = 17.1 Hz), 113.2, 106.7, 68.0, 52.4, 43.4, 37.3, 37.2, 30.5, 28.6, 23.6, 19.6. HRMS-ESI: calculated for $\text{C}_{20}\text{H}_{25}\text{F}_2\text{N}_3$ $[\text{M} + \text{H}]^+$ 346.2089, found 346.2091.

NOS Enzyme Inhibition Assay. The NOS inhibitory activity of **21** was measured by the hemoglobin (Hb) NO capture assay following a protocol described previously.^{26,36} Briefly, the assay was done in 100 mM 4-(2-hydroxyethyl)-1-piperazine-ethanesulfonic acid (HEPES) buffer with 10% glycerol (pH 7.4) at 37 °C in the presence of 10 μM L-Arg, 10 μM H₄B, 100 μM NADPH, 0.83 mM CaCl₂, 320 units/mL calmodulin, and 3 μM human oxyhemoglobin. The concentration of L-Arg, 10 μM , was used as it is sufficient not to cause NOS uncoupling and is close to the K_m values of all three NOS isoforms where competitive inhibitors can be detected effectively. The assay was performed in 96-well plates using a Biotek Gen5 microplate reader. NO production was kinetically monitored at 401 nm for 6 min. Rat nNOS,³⁷ human nNOS,³⁸ murine macrophage iNOS,³⁹ human iNOS,⁴⁰ and human eNOS⁴¹ are expressed in *Escherichia coli* and purified as previously reported. The inhibition constants (K_i) for all NOSs were calculated from the IC₅₀ values of the dose–response curves using the Cheng–Prusoff equation: $K_i = \text{IC}_{50}/(1 + [\text{S}]/K_m)$ ⁴² and K_m (human nNOS: 1.6 μM ; rat nNOS: 1.3 μM ; murine iNOS: 8.2 μM ; bovine eNOS: 1.7 μM ; human eNOS: 3.9 μM ; human iNOS: 8.0 μM).^{43,44} Dose–response curves were constructed from seven to nine test concentrations (200 μM to 50 nM), and IC₅₀ values were calculated by nonlinear regression using GraphPad Prism software.

The calculated standard deviations from dose–response curves of the assays were less than 10% with all NOSs.

PAMPA-BBB Assay. The PAMPA-BBB assay was performed following a protocol described previously.²⁶ Briefly, the assay was done in 10 mM phosphate-buffered saline (PBS) buffer (pH 7.5), and compounds were tested at a concentration of 200 μ M. The donor plate was first coated with 4 μ L of porcine brain lipid (20 mg/mL in dodecane), followed by an addition of 250 μ L of a test compound. The acceptor plate was filled with 250 μ L of PBS, and the donor plate was carefully placed on top of the acceptor plate to make a “sandwich”. The plate was incubated at 25 °C for 17 h in a saturated humidity atmosphere with an orbital agitation at 100 rpm. Verapamil and theophylline were used as a positive and a negative control, respectively. After incubation, 150 μ L of test solution was taken from each well from both sides (donor and acceptor) and transferred to the UV plate for measurement. The effective permeability (P_e) was calculated using the following equation:^{4,5}

$$P_e = \frac{2.303}{A \cdot (t - \tau_{ss})} \cdot \frac{V_A \cdot V_D}{(V_A + V_D)} \lg \left[1 - \left(\frac{V_A + V_D}{(1-R) \cdot V_D} \right) \cdot \left(\frac{C_A(t)}{C_D(0)} \right) \right],$$
 where P_e is the effective permeability (cm s^{-1}); V_A and V_D are the volume of the acceptor and donor wells (0.25 cm^3), respectively; $C_A(t)$ is the concentration of the acceptor well at time t ; $C_D(0)$ and $C_D(t)$ are the concentrations of the donor well at t_0 and t , respectively; A is the filter well area (0.21 cm^2); t is the incubation time (s); τ_{ss} is the time to reach a steady state (usually very short compared with the incubation time); and R is the retention membrane factor and was calculated using the following equation: $R = \left[1 - \frac{C_D(t)}{C_D(0)} - \frac{V_A}{V_D} \cdot \frac{C_A(t)}{C_D(0)} \right]$. P_e was reported as an average of triplicate with a standard deviation.

Caco-2 Assay. The bidirectional Caco-2 assay was performed by Sai Life Sciences, Pune, India, or Chempartner, Shanghai, China. Briefly, the assay was done in Hank's balanced salt solution buffer (pH 7.4) in 90 min at 37 °C. Compounds were tested at a concentration of 5 μ M (0.1% dimethyl sulfoxide). Studied compounds were applied to either the apical ($A \rightarrow B$ direction) or the basal ($B \rightarrow A$ direction) side. The apparent permeability (P_{app}) was calculated using the following equation: $P_{app} = (dQ/dt)/C_0A$, where dQ/dt is the change of test compound concentration in the receiver chamber over time, C_0 is the initial concentration of the compounds in the donor well, and A is the filter well area (0.7 cm^2). The efflux ratio is defined by the ratio of the apparent permeability of $B \rightarrow A$ over that of $A \rightarrow B$. An ER value above 2.5 indicates that a compound is possibly a substrate of P-gp or other active efflux transporters.

Expression and Purification of Full-Length hiNOS. The plasmid of human iNOS with an N-terminal 6-His tag built in a pCWori vector was a generous gift from Dr. Paul R. Ortiz de Montellano's laboratory (University of California, San Francisco). The *E. coli* competent cells BL21(DE3) were first transformed with the plasmid of human CaM to prepare the CaM-plasmid-containing competent cells, which were then transformed a second time with the hiNOS plasmid and grown on an agar plate containing both ampicillin and chloramphenicol. The resulting colonies were used to inoculate the overnight Luria-Bertani culture containing both antibiotics. On the next day, each 1 L of terrific broth culture (containing 0.5 mM CaCl_2) was inoculated with 2 mL of starter culture in the presence of 100 μ g/mL ampicillin and 35 μ g/mL chloramphenicol. The incubation was continued at 37 °C with 220 rpm shaking until the optical density at 600 nm reached 2.0 or higher. At that time, the protein expression was induced with 0.5 mM isopropyl β -D-1-thiogalactopyranoside, 0.4 mM δ -aminolevulinic acid, and 3 μ M riboflavin. The incubation was continued for another 40 h at 25 °C and 100 rpm before cell harvesting. The hiNOS protein purification protocols were similar to those³⁸ used for both hnNOS and heNOS through two affinity columns, Ni nitrilotriacetic acid and 2',5'-adenosine diphosphate (2',5'-ADP) Sepharose, in sequence. To remove the oxidized nicotinamide adenine dinucleotide phosphate used in the ADP column elution, the final step of purification was either a Superdex 200 column (GE Healthcare) or simply a small desalting column (10DG, BioRad) depending on the purity of the protein from the earlier two columns. The coexpression and copurification with CaM

are crucial for the proper folding of the full-length hiNOS that uses CaM as a tightly bound subunit.

Inhibitor Complex Crystal Preparation. The sitting drop vapor diffusion method was used to grow crystals at 4 °C for the heme domains of rnNOS (8 mg/mL containing 20 mM histidine), the hnNOS K301R/R354A/G357D mutant (10 mg/mL), and heNOS (7 mg/mL). The crystal growth conditions were as described previously.³⁸ The only exception is that the pH for the heNOS crystal growth is 7.5 rather than 6.5 as mistakenly reported there. Fresh crystals were first passed stepwise through cryoprotectant solutions. The pH of the final soaking solution for rnNOS was adjusted from 5.8 to 6.5, 7.0 (in 2-(*N*-morpholino)ethanesulfonic acid), and 7.5 (in HEPES) and that for hnNOS from 7.2 to 7.5 (in HEPES), and for heNOS, the Bis-Tris buffer at pH 7.5 was unchanged. At pH 7.5, crystals were soaked with 5–10 mM inhibitor for 2–4 h at 4 °C before being flash cooled with liquid nitrogen and stored until data collection. The presence of an acetate ion near the heme active site in bovine eNOS caused interference in the binding mode of some inhibitors. The high concentration of magnesium acetate in the heNOS growth conditions may also introduce an acetate near the active site that may influence the binding mode of inhibitors.⁴⁶ To avoid having this acetate in the structure, the 250 mM magnesium acetate in the crystallization well solution was replaced with 100 mM MgCl_2 in the cryosoaking solution.

X-ray Diffraction Data Collection, Data Processing, and Structural Refinement. The cryogenic (100 K) X-ray diffraction data were collected remotely at the Stanford Synchrotron Radiation Lightsource (SSRL) or Advanced Light Source (ALS) through data collection control software Blu-Ice⁴⁷ and a crystal-mounting robot. When a charge-coupled device (CCD) detector was used, 100–125° of data were typically collected with 0.5° per frame. If a Pilatus pixel array detector was used, 140–160° of fine-sliced data were collected with 0.2° per frame. Raw CCD data frames were indexed, integrated, and scaled using iMOSFLM,⁴⁸ but the pixel array data were preferably processed with XDS⁴⁹ and scaled with Aimless.⁵⁰ The binding of inhibitors was detected by initial difference Fourier maps calculated with REFMAC.⁵¹ The inhibitor molecules were then modeled in Coot⁵² and refined using REFMAC or PHENIX.⁵³ The crystal packing of the MgCl_2 -soaked heNOS crystals was changed slightly, resulting in a symmetry change from the orthorhombic $P2_12_12_1$ reported previously³⁸ to monoclinic $P2_1$, with a β angle only 0.6–0.7° off compared to the original 90°. Therefore, a molecular replacement calculation with PHASER-MR⁵⁴ was needed to solve the structure. In the $P2_1$ space group, there are two heNOS dimers in the asymmetric unit. Disordering in portions of inhibitors bound in the NOS active sites was often observed, sometimes resulting in poor density quality. However, partial structural features were usually still visible if the contour level of the sigmaA weighted $2m|F_o| - D|F_c|$ map was dropped to 0.5σ , which afforded the building of reasonable models into the disordered regions. Water molecules were added in PHENIX and checked by Coot. The TLS⁵⁵ protocol was implemented in the PHENIX refinements with each subunit as one TLS group. The omit $F_o - F_c$ density maps were calculated by the Polder map facility in PHENIX for the bound inhibitors.⁵⁶ The refined structures were validated in Coot before deposition in the Protein Data Bank. The crystallographic data collection and refinement statistics are reported in Table S2.

■ ASSOCIATED CONTENT

Supporting Information

The Supporting Information is available free of charge on the ACS Publications website at DOI: 10.1021/acs.jmedchem.8b02032.

Crystal structures of rat nNOS with compounds 2–7, 10–15, and 17–20 and heNOS with compounds 2, 4, 6, 8, 9, 11, 13, and 14; crystallographic data collection and refinement statistics for rat nNOS, human nNOS, and human eNOS; predicted physicochemical properties of

1–21, detailed synthetic procedures and analytical data for all precursors and intermediates; HPLC traces of compounds 2–21 (PDF)

Molecular formula strings (CSV)

Accession Codes

PDB codes for X-ray structures described in this study are as follow: hnNOS-2, 6NG1; hnNOS-3, 6NG2; hnNOS-4, 6NG4; hnNOS-5, 6NG5; hnNOS-6, 6NG6; hnNOS-9, 6NG7; hnNOS-10, 6NG8; hnNOS-11, 6NGA; hnNOS-12, 6NGB; hnNOS-13, 6NGC; hnNOS-14, 6NGD; hnNOS-15, 6NGE; hnNOS-17, 6NGF; hnNOS-18, 6NGH; hnNOS-19, 6NGI; hnNOS-20, 6NHB; hnNOS-21, 6NHC; rnNOS-2, 6NGJ; rnNOS-3, 6NGK; rnNOS-4, 6NGL; rnNOS-5, 6NGM; rnNOS-6, 6NGN; rnNOS-7, 6NGP; rnNOS-8, 6NGQ; rnNOS-9, 6NGR; rnNOS-10, 6NGS; rnNOS-11, 6NGT; rnNOS-12, 6NGU; rnNOS-13, 6NGV; rnNOS-14, 6NGW; rnNOS-15, 6NGX; rnNOS-17, 6NGY; rnNOS-18, 6NGZ; rnNOS-19, 6NH0; rnNOS-20, 6NHE; rnNOS-21, 6NHD; heNOS-2, 6NH1; heNOS-4, 6NH2; heNOS-6, 6NH3; heNOS-8, 6NH4; heNOS-9, 6NH5; heNOS-11, 6NH6; heNOS-13, 6NH7; heNOS-14, 6NH8; heNOS-21, 6NHF.

AUTHOR INFORMATION

Corresponding Authors

*E-mail: poulos@uci.edu. Tel: +1 949 824 7020 (T.L.P.).

*E-mail: Agman@chem.northwestern.edu. Tel: +1 847 491 5653. Fax: +1 847 491 7713 (R.B.S.).

ORCID

Thomas L. Poulos: 0000-0002-5648-3510

Richard B. Silverman: 0000-0001-9034-1084

Notes

The authors declare no competing financial interest.

ACKNOWLEDGMENTS

We are grateful for the generous support from the National Institutes of Health (R01 GM049725 to R.B.S., GM057353 to T.L.P.). This work made use of the IMSERC at Northwestern University, which has received support from the Soft and Hybrid Nanotechnology Experimental (SHyNE) Resource (NSF NNCI-1542205); the State of Illinois and International Institute for Nanotechnology (IIN). We also thank the beamline staff at SSRL and ALS for their assistance during the remote X-ray diffraction data collections. H.L. would like to thank Carla Plaza for her assistance in protein preparations, which provided samples for both the structure determinations and the inhibitory assays.

ABBREVIATIONS

NO, nitric oxide; nNOS, neuronal nitric oxide synthase; iNOS, inducible nitric oxide synthase; eNOS, endothelial nitric oxide synthase; rnNOS, rat neuronal nitric oxide synthase; hnNOS, human neuronal nitric oxide synthase; hiNOS, human inducible nitric oxide synthase; heNOS, human endothelial nitric oxide synthase; L-Arg, L-arginine; 2',5'-ADP, 2',5'-adenosine diphosphate; CaM, calmodulin; DNA, deoxyribonucleic acid; H₄B, (6R)-5,6,7,8-tetrahydrobiopterin; HEPES, 4-(2-hydroxyethyl)-1-piperazine-ethanesulfonic acid; NADPH, reduced nicotinamide adenine dinucleotide phosphate; BBB, blood–brain barrier; CNS, central nervous system; PAMPA, parallel artificial membrane permeability assay; P-gp, P-

glycoprotein; BCRP, breast-cancer-resistant protein; ER, efflux ratio; P_e, effective permeability; P_{app}, apparent permeability

REFERENCES

- (1) Gribkoff, V. K.; Kaczmarek, L. K. The need for new approaches in CNS drug discovery: Why drugs have failed, and what can be done to improve outcomes. *Neuropharmacology* **2017**, *120*, 11–19.
- (2) Nutt, D. J.; Attridge, J. CNS drug development in Europe — past progress and future challenges. *Neurobiol. Dis.* **2014**, *61*, 6–20.
- (3) Di, L.; Rong, H.; Feng, B. Demystifying brain penetration in central nervous system drug discovery. *J. Med. Chem.* **2013**, *56*, 2–12.
- (4) Banks, W. A. From blood–brain barrier to blood–brain interface: new opportunities for CNS drug delivery. *Nat. Rev. Drug Discovery* **2016**, *15*, 275.
- (5) Löscher, W.; Potschka, H. Drug resistance in brain diseases and the role of drug efflux transporters. *Nat. Rev. Neurosci.* **2005**, *6*, 591.
- (6) Di, L.; Kerns, E. H. *Drug-like Properties: Concepts, Structure Design, and Methods from ADME to Toxicity Optimization*, 2nd ed.; Elsevier: Amsterdam, 2016; p 329.
- (7) Rankovic, Z. CNS drug design: balancing physicochemical properties for optimal brain exposure. *J. Med. Chem.* **2015**, *58*, 2584–2608.
- (8) Maccallini, C.; Amoroso, R. Targeting neuronal nitric oxide synthase as a valuable strategy for the therapy of neurological disorders. *Neural Regener. Res.* **2016**, *11*, 1731–1734.
- (9) Drechsel, D. A.; Estévez, A. G.; Barbeito, L.; Beckman, J. S. Nitric oxide-mediated oxidative damage and the progressive demise of motor neurons in ALS. *Neurotoxic. Res.* **2012**, *22*, 251–264.
- (10) de la Torre, J. C.; Stefano, G. B. Evidence that Alzheimer's disease is a microvascular disorder: the role of constitutive nitric oxide. *Brain Res. Rev.* **2000**, *34*, 119–136.
- (11) Garthwaite, J.; Boulton, C. L. Nitric oxide signaling in the central nervous system. *Annu. Rev. Physiol.* **1995**, *57*, 683–706.
- (12) Uehara, T.; Nakamura, T.; Yao, D.; Shi, Z.-Q.; Gu, Z.; Ma, Y.; Masliah, E.; Nomura, Y.; Lipton, S. A. S-Nitrosylated protein-disulphide isomerase links protein misfolding to neurodegeneration. *Nature* **2006**, *441*, 513–517.
- (13) Li, J.; Wuliji, O.; Li, W.; Jiang, Z.-G.; Ghanbari, H. A. Oxidative stress and neurodegenerative disorders. *Int. J. Mol. Sci.* **2013**, *14*, 24438–24475.
- (14) Chen, X.; Guo, C.; Kong, J. Oxidative stress in neurodegenerative diseases. *Neural Regener. Res.* **2012**, *7*, 376–385.
- (15) Torreilles, F.; Salman-Tabcheh, S.; Guérin, M.-C.; Torreilles, J. Neurodegenerative disorders: the role of peroxynitrite. *Brain Res. Rev.* **1999**, *30*, 153–163.
- (16) Bolaños, J. P.; Almeida, A.; Stewart, V.; Peuchen, S.; Land, J. M.; Clark, J. B.; Heales, S. J. R. Nitric oxide-mediated mitochondrial damage in the brain: mechanisms and implications for neurodegenerative diseases. *J. Neurochem.* **1997**, *68*, 2227–2240.
- (17) Mukherjee, P.; Cinelli, M. A.; Kang, S.; Silverman, R. B. Development of nitric oxide synthase inhibitors for neurodegeneration and neuropathic pain. *Chem. Soc. Rev.* **2014**, *43*, 6814–6838.
- (18) Silverman, R. B. Design of selective neuronal nitric oxide synthase inhibitors for the prevention and treatment of neurodegenerative diseases. *Acc. Chem. Res.* **2009**, *42*, 439–451.
- (19) Alderton, W. K.; Cooper, C. E.; Knowles, R. G. Nitric oxide synthases: structure, function and inhibition. *Biochem. J.* **2001**, *357*, 593–615.
- (20) Moore, P. K.; Handy, R. L. C. Selective inhibitors of neuronal nitric oxide synthase — is no NOS really good NOS for the nervous system? *Trends Pharmacol. Sci.* **1997**, *18*, 204–211.
- (21) Li, H.; Wang, H.-Y.; Kang, S.; Silverman, R. B.; Poulos, T. L. Electrostatic control of isoform selective inhibitor binding in nitric oxide synthase. *Biochemistry* **2016**, *55*, 3702–3707.
- (22) Barbanti, P.; Egeo, G.; Aurilia, C.; Fofi, L.; Della-Morte, D. Drugs targeting nitric oxide synthase for migraine treatment. *Expert Opin. Invest. Drugs* **2014**, *23*, 1141–1148.
- (23) Ji, H.; Stanton, B. Z.; Igarashi, J.; Li, H.; Martásek, P.; Roman, L. J.; Poulos, T. L.; Silverman, R. B. Minimal pharmacophoric

elements and fragment hopping, an approach directed at molecular diversity and isozyme selectivity. design of selective neuronal nitric oxide synthase inhibitors. *J. Am. Chem. Soc.* **2008**, *130*, 3900–3914.

(24) Kang, S.; Li, H.; Tang, W.; Martásek, P.; Roman, L. J.; Poulos, T. L.; Silverman, R. B. 2-Aminopyridines with a truncated side chain to improve human neuronal nitric oxide synthase inhibitory potency and selectivity. *J. Med. Chem.* **2015**, *58*, 5548–5560.

(25) Wang, H.-Y.; Qin, Y.; Li, H.; Roman, L. J.; Martásek, P.; Poulos, T. L.; Silverman, R. B. Potent and selective human neuronal nitric oxide synthase inhibition by optimization of the 2-aminopyridine-based scaffold with a pyridine linker. *J. Med. Chem.* **2016**, *59*, 4913–4925.

(26) Do, H. T.; Wang, H.-Y.; Li, H.; Chreifi, G.; Poulos, T. L.; Silverman, R. B. Improvement of cell permeability of human neuronal nitric oxide synthase inhibitors using potent and selective 2-aminopyridine-based scaffolds with a fluorobenzene linker. *J. Med. Chem.* **2017**, *60*, 9360–9375.

(27) Wager, T. T.; Hou, X.; Verhoest, P. R.; Villalobos, A. Moving beyond rules: the development of a central nervous system multiparameter optimization (CNS MPO) approach to enable alignment of druglike properties. *ACS Chem. Neurosci.* **2010**, *1*, 435–449.

(28) Di, L.; Kerns, E. H.; Fan, K.; McConnell, O. J.; Carter, G. T. High throughput artificial membrane permeability assay for blood–brain barrier. *Eur. J. Med. Chem.* **2003**, *38*, 223–232.

(29) Di, L.; Kerns, E. H.; Bezar, I. F.; Petusky, S. L.; Huang, Y. Comparison of blood–brain barrier permeability assays: in situ brain perfusion, MDR1-MDCKII and PAMPA-BBB. *J. Pharm. Sci.* **2009**, *98*, 1980–1991.

(30) Davis, T. P.; Sanchez-Covarubias, L.; Tome, M. E. P-glycoprotein trafficking as a therapeutic target to optimize CNS drug delivery. *Adv. Pharmacol.* **2014**, *71*, 25–44.

(31) Patil, A. G.; D'Souza, R.; Dixit, N.; Damre, A. Validation of quinidine as a probe substrate for the in vitro P-gp inhibition assay in Caco-2 cell monolayer. *Eur. J. Drug Metab. Pharmacokinet.* **2011**, *36*, 115.

(32) Delker, S. L.; Xue, F.; Li, H.; Jamal, J.; Silverman, R. B.; Poulos, T. L. Role of zinc in isoform-selective inhibitor binding to neuronal nitric oxide synthase. *Biochemistry* **2010**, *49*, 10803–10810.

(33) Perry, J. M.; Zhao, Y.; Marletta, M. A. Cu²⁺ and Zn²⁺ inhibit nitric-oxide synthase through an interaction with the reductase domain. *J. Biol. Chem.* **2000**, *275*, 14070–14076.

(34) Wang, Z.-Q.; Tejero, J.; Wei, C.-C.; Haque, M. M.; Santolini, J.; Fadlalla, M.; Biswas, A.; Stuehr, D. J. Arg375 tunes tetrahydrobiopterin functions and modulates catalysis by inducible nitric oxide synthase. *J. Inorg. Biochem.* **2012**, *108*, 203–215.

(35) St. Jean, D. J.; Fotsch, C. Mitigating heterocycle metabolism in drug discovery. *J. Med. Chem.* **2012**, *55*, 6002–6020.

(36) Hevel, J. M.; Marletta, M. A. Nitric-oxide synthase assays. *Methods Enzymol.* **1994**, *233*, 250–258.

(37) Roman, L. J.; Sheta, E. A.; Martasek, P.; Gross, S. S.; Liu, Q.; Masters, B. S. High-level expression of functional rat neuronal nitric oxide synthase in *Escherichia coli*. *Proc. Natl. Acad. Sci.* **1995**, *92*, 8428–8432.

(38) Li, H.; Jamal, J.; Plaza, C.; Pineda, S. H.; Chreifi, G.; Jing, Q.; Cinelli, M. A.; Silverman, R. B.; Poulos, T. L. Structures of human constitutive nitric oxide synthases. *Acta Crystallogr., Sect. D: Biol. Crystallogr.* **2014**, *70*, 2667–2674.

(39) Hevel, J. M.; White, K. A.; Marletta, M. A. Purification of the inducible murine macrophage nitric oxide synthase. Identification as a flavoprotein. *J. Biol. Chem.* **1991**, *266*, 22789–22791.

(40) Li, H.; Raman, C. S.; Glaser, C. B.; Blasko, E.; Young, T. A.; Parkinson, J. F.; Whitlow, M.; Poulos, T. L. Crystal structures of zinc-free and -bound heme domain of human inducible nitric-oxide synthase: implications for dimer stability and comparison with endothelial nitric-oxide synthase. *J. Biol. Chem.* **1999**, *274*, 21276–21284.

(41) Fischmann, T. O.; Hruza, A.; Niu, X. D.; Fossetta, J. D.; Lunn, C. A.; Dolphin, E.; Prongay, A. J.; Reichert, P.; Lundell, D. J.; Narula,

S. K.; Weber, P. C. Structural characterization of nitric oxide synthase isoforms reveals striking active-site conservation. *Nat. Struct. Biol.* **1999**, *6*, 233.

(42) Cheng, Y.-C.; Prusoff, W. H. Relationship between the inhibition constant (K_i) and the concentration of inhibitor which causes 50 percent inhibition (IC₅₀) of an enzymatic reaction. *Biochem. Pharmacol.* **1973**, *22*, 3099–3108.

(43) Leber, A.; Hemmens, B.; Klösch, B.; Goessler, W.; Raber, G.; Mayer, B.; Schmidt, K. Characterization of recombinant human endothelial nitric-oxide synthase purified from the yeast *pichia pastoris*. *J. Biol. Chem.* **1999**, *274*, 37658–37664.

(44) Fossetta, J. D.; Niu, X. D.; Lunn, C. A.; Zavodny, P. J.; Narula, S. K.; Lundell, D. Expression of human inducible nitric oxide synthase in *Escherichia coli*. *FEBS Lett.* **1996**, *379*, 135–138.

(45) Müller, J.; Esső, K.; Dargó, G.; Könczöl, Á.; Balogh, G. T. Tuning the predictive capacity of the PAMPA-BBB model. *Eur. J. Pharm. Sci.* **2015**, *79*, 53–60.

(46) Cinelli, M. A.; Li, H.; Pensa, A. V.; Kang, S.; Roman, L. J.; Martásek, P.; Poulos, T. L.; Silverman, R. B. Phenyl ether- and aniline-containing 2-aminoquinolines as potent and selective inhibitors of neuronal nitric oxide synthase. *J. Med. Chem.* **2015**, *58*, 8694–8712.

(47) McPhillips, T. M.; McPhillips, S. E.; Chiu, H.-J.; Cohen, A. E.; Deacon, A. M.; Ellis, P. J.; Garman, E.; Gonzalez, A.; Sauter, N. K.; Phizackerley, R. P.; Soltis, S. M.; Kuhn, P. Blu-ice and the distributed control system: software for data acquisition and instrument control at macromolecular crystallography beamlines. *J. Synchrotron Radiat.* **2002**, *9*, 401–406.

(48) Batty, T. G. G.; Kontogiannis, L.; Johnson, O.; Powell, H. R.; Leslie, A. G. W. iMOSFLM: a new graphical interface for diffraction-image processing with MOSFLM. *Acta Crystallogr., Sect. D: Biol. Crystallogr.* **2011**, *67*, 271–281.

(49) Kabsch, W. XDS. *Acta Crystallogr., Sect. D: Biol. Crystallogr.* **2010**, *66*, 125–132.

(50) Evans, P. Scaling and assessment of data quality. *Acta Crystallogr., Sect. D: Struct. Biol.* **2006**, *62*, 72–82.

(51) Murshudov, G. N.; Vagin, A. A.; Dodson, E. J. Refinement of macromolecular structures by the maximum-likelihood method. *Acta Crystallogr., Sect. D: Struct. Biol.* **1997**, *53*, 240–255.

(52) Emsley, P.; Cowtan, K. Coot: model-building tools for molecular graphics. *Acta Crystallogr., Sect. D: Biol. Crystallogr.* **2004**, *60*, 2126–2132.

(53) Adams, P. D.; Afonine, P. V.; Bunkoczi, G.; Chen, V. B.; Davis, I. W.; Echols, N.; Headd, J. J.; Hung, L.-W.; Kapral, G. J.; Grosse-Kunstleve, R. W.; McCoy, A. J.; Moriarty, N. W.; Oeffner, R.; Read, R. J.; Richardson, D. C.; Richardson, J. S.; Terwilliger, T. C.; Zwart, P. H. PHENIX: a comprehensive Python-based system for macromolecular structure solution. *Acta Crystallogr., Sect. D: Struct. Biol.* **2010**, *66*, 213–221.

(54) McCoy, A. J.; Grosse-Kunstleve, R. W.; Adams, P. D.; Winn, M. D.; Storoni, L. C.; Read, R. J. Phaser crystallographic software. *J. Appl. Crystallogr.* **2007**, *40*, 658–674.

(55) Winn, M. D.; Isupov, M. N.; Murshudov, G. N. Use of TLS parameters to model anisotropic displacements in macromolecular refinement. *Acta Crystallogr., Sect. D: Struct. Biol.* **2001**, *57*, 122–133.

(56) Liebschner, D.; Afonine, P. V.; Moriarty, N. W.; Poon, B. K.; Sobolev, O. V.; Terwilliger, T. C.; Adams, P. D. Polder maps: improving OMIT maps by excluding bulk solvent. *Acta Crystallogr., Sect. D: Struct. Biol.* **2017**, *73*, 148–157.